Reactive oxygen species rescue lysosome coalescence during PIKfyve inhibition

Golam T. Saffi[1,2], Evan Tang[2], Aaron Fountain[1,2] and Roberto J. Botelho[1,2,*]

[1]Molecular Science Graduate Program and [2]Department of Chemistry and Biology, Ryerson University, Toronto, Ontario, Canada

[*]To whom correspondence should be sent to: rbotelho@ryerson.ca

Keywords

Lysosomes, reactive oxygen species, membrane trafficking, organelles, fusion, fission, cytoskeleton

Abbreviations

CDNB: 1-chloro-2,4,-dinitrobenzene; MCB: monochlorobimane; NAC: N-acetyl-L-cysteine; PFA: paraformaldehyde; PtdInsP: phosphoinositide; PtdIns(3,5)P2: phosphatidylinositol-3,5-bisphosphate; ROS: reactive oxygen species

Acknowledgement:

ARPE-1 (RPE) cells stably expressing clathrin heavy chain-eGFP were a kind gift from Dr. Costin Antonescu. We would also like to thank Mr. Janusan Baskararajah for technical assistance.

Abstract

Lysosomes are terminal, degradative organelles of the endosomal pathway that undergo repeated fusion-fission cycles with themselves and other organelles like endosomes, phagosomes, and autophagosomes. Lysosome number, size and degradative flux depends on the equilibrium between fusion and fission rates. Thus, conditions that favour fusion over fission will reduce lysosome numbers while enlarging remaining lysosomes. Conversely, conditions that favour fission over fusion will cause lysosome fragmentation and increase their numbers. PIKfyve is a phosphoinositide kinase that generates phosphatidylinositol-3,5-bisphosphate to modulate several lysosomal functions. PIKfyve inhibition causes a dramatic increase in lysosome size and reduction in lysosome number, consistent with lysosome coalescence. This is thought to proceed through reduced lysosome reformation and/or fission after fusion with endosomes or other lysosomes. Previously, we observed that photo-damage during live-cell imaging prevented lysosome coalescence during acute PIKfyve inhibition. Thus, we postulated that lysosome fusion and/or fission dynamics are affected by reactive oxygen species (ROS). Here, we show that ROS generated by four independent mechanisms all arrested lysosome coalescence during PIKfyve inhibition and accelerated lysosome fragmentation during PIKfyve re-activation. However, depending on the ROS species and/or mode of production, lysosome dynamics were affected distinctly. H_2O_2 impaired lysosome motility and reduced lysosome fusion with phagosomes, suggesting that H_2O_2 prevents lysosome coalescence in PIKfyve-impaired cells by reducing lysosome fusogenecity. In comparison, inhibitors of oxidative phosphorylation, glutathione, and thioredoxin that produce superoxide, did not impair lysosome motility but instead promoted clearance of actin puncta on lysosomes formed during PIKfyve inhibition.

Additionally, actin depolymerizing agents prevented lysosome coalescence during PIKfyve inhibition. Thus, we discovered that ROS can generally prevent lysosome coalescence during PIKfyve inhibition using distinct mechanisms.

Introduction

Lysosomes are typically defined as terminal organelles with an acidic and degradative lumen that digest macromolecules received through endocytosis, phagocytosis and autophagy (Luzio et al., 2000; Luzio et al., 2007; Pu et al., 2016). In reality, lysosomes are part of an endomembrane spectrum formed through heterotypic and homotypic fusion between late endosomes that enclose cargo for degradation, terminal lysosomes, which are non-acidic, hydrolase-dormant storage organelles, and endolysosomes, hybrids formed when late endosomes and terminal lysosomes fuse together (Bissig et al., 2017; Bright et al., 1997; Bright et al., 2016; Ward et al., 1997); we use the term *lysosome* to refer to this spectrum. Importantly, fusion and content exchange along the lysosomal spectrum proceeds through two major routes. First, lysosomes can fuse with a target organelle resulting in complete merger of the two compartments. Alternatively, lysosomes can exchange content with another target organelle through "kiss-and-run"; in this process, a transient fusion between two organelles generates an aqueous pore to exchange content, and is followed by fission to prevent amalgamation of the two compartments (Bright et al., 2005; Bright et al., 2016; Duclos, 2003; Saffi and Botelho, 2019).

Delivery of cargo to lysosomes is an incessant process that depends on cargo sorting, membrane targeting, and the fusion machinery, which are governed by, among others, the lysosomal GTPases Rab7 and Arl8b GTPases (Khatter et al., 2015; Wang et al., 2011). These GTPases modulate the movement of lysosomes along microtubule tracks through their effectors; Rab7 uses RILP and FYCO1 to engage dynein and kinesins, thus moving lysosomes towards the cell centre and periphery, respectively (Cantalupo et al., 2001; Pankiv et al., 2010). In comparison, Arl8b uses SKIP to engage kinesin to promote lysosome positioning to the cell periphery (Rosa-Ferreira and Munro, 2011). When lysosomes contact other lysosomes/late

endosomes, this engages tethering complexes like HOPS, also modulated by Rab7 and Arl8b, and eventual fusion via VAMP7 and syntaxin-7 SNAREs (Khatter et al., 2015; Luzio et al., 2009; Wang et al., 2011). Lysosome fusion and fission dynamics is also modulated by intralysosomal Ca^{2+} release via TRPML1 and P2X4 (Cao et al., 2015; Cao et al., 2017).

Despite the incessant fusion of content to lysosomes, cells maintain lysosome number and size, suggesting that fission and exit of cargo is also relentless. Yet, much less is known about lysosome fission, which can proceed through vesiculation, tubulation, and splitting (Saffi and Botelho, 2019). Lysosome fission mechanisms may include classical coat and fission machinery such as clathrin and dynamin, adaptor protein (AP1-AP5) complexes, putative coat proteins like spastizin and spatacsin, and actin assemblies (Fang et al., 2016; Hong et al., 2015; Renvoisé et al., 2014; Rong et al., 2012; Saffi and Botelho, 2019; Traub et al., 1996). Coordination of these fission machineries is poorly understood but likely involves TRPML1-Ca^{2+} release, which in turn controls calmodulin and mTORC1 (Cao et al., 2017; Li et al., 2016; Yang et al., 2019). For example, mTORC1 is required for phagosome and lysosome shrinkage and resolution (Krajcovic et al., 2013; Yang et al., 2019). Additionally, phosphoinositides (PtdInsPs) play a key role in lysosome fission dynamics including modulation of vesiculation versus tubulation (Saffi and Botelho, 2019). Amongst these, lysosome fission-fusion cycles are coordinated by the PIKfyve lipid kinase that synthesizes phosphatidylinositol-3,5-bisphosphate [PtdIns(3,5)P_2] and perhaps phosphatidylinositol-5-phosphate (McCartney et al., 2014; Shisheva et al., 2015). Pharmacological or genetic disruption of PIKfyve and partner proteins like Vac14 and the Fig4 phosphatase cause enlarged lysosomes, partly by impairing fission and reformation of terminal lysosomes (Bissig et al., 2017; Chow et al., 2007; Choy et al., 2018; McCartney et al., 2014; Sbrissa et al., 2007). The result is lysosome coalescence, enlarging lysosomes while

reducing their numbers (Bissig et al., 2017; Choy et al., 2018). It remains unclear how PIKfyve controls lysosome fission but may involve control of actin-assembly on lysosomes, coordination of TRPML1-Ca^{2+}-calmodulin, and regulation of Atg18/WIPI proteins (Cao et al., 2017; Gopaldass et al., 2017; Hong et al., 2015; Yang et al., 2019).

During our studies with acute PIKfyve inhibition, we observed that imaging by spinning disc confocal microscopy at high frequency inhibited lysosome enlargement caused by PIKfyve inhibition (Choy et al., 2018). We speculated that this resulted from photo-generated reactive oxygen species (ROS), which can include formation of superoxide anion (O_2^-), hydrogen peroxide (H_2O_2), and hydroxyl radical ($OH\cdot$) (Chen et al., 2009; Dizdaroglu and Jaruga, 2012; Finkel, 2012). ROS species are also formed as part of normal aerobic metabolism and can actually be produced as signaling intermediates to modulate cell proliferation and the inflammatory response (Ristow and Schmeisser, 2011; Schieber and Chandel, 2014). Yet, overt ROS production is detrimental, damaging proteins, lipids, and DNA. Thus, cells have evolved multiple systems to quench ROS levels such as O_2^- dismutase, catalase, glutathione, and thioredoxin (Marengo et al., 2016; Schieber and Chandel, 2014). In addition, autophagy and the lysosomal systems play key roles in resolving ROS damage. Indeed, ROS exposure activates TRPML1 to release intralysosomal Ca^{2+}, induce lysosome-autophagosome fusion, and stimulate the transcription factor TFEB to enhance lysosome and autophagy gene expression (Zhang et al., 2016).

In this study, we sought to understand if other modes of ROS generation could abate lysosome coalescence during PIKfyve inhibition and to better define the mechanisms of action. Strikingly, we found that different sources of ROS reduced lysosome coalescence during PIKfyve inhibition and accelerated lysosome fragmentation upon PIKfyve reactivation.

Interestingly, these distinct ROS hindered lysosome coalescence differently. H_2O_2 prevented lysosome coalescence by impairing lysosome motility and blunting lysosome fusogenecity. In comparison, oxidative decoupling of the mitochondria with rotenone and inhibitors of glutathione and thioredoxin counteracted lysosome coalescence by releasing actin clusters that accumulated on lysosomes during PIKfyve impairment.

Materials and Methods

Cell culture, plasmids, and transfection

RAW 264.7 macrophages and HeLa cells were grown in Dulbecco's Modified Eagle Medium (DMEM; Wisent, St Bruno, QC) supplemented with 5% heat-inactivated fetal bovine serum (FBS; Wisent). ARPE-1 (RPE) cells stably expressing clathrin heavy chain-eGFP were grown in DMEM/F12 medium (Gibco) supplemented with 10% FBS (Aguet et al., 2013). All cells were grown at 5% CO_2 and 37 ºC and routinely checked for contamination. FuGene HD (Promega, Madison, WI) was used for transient transfections following manufacturer's instructions with a ratio of 3:1 FuGene HD transfection reagent (µl) to DNA (µg). The transfection mixture was replaced with fresh complete medium 4-5 h post-transfection and cells were used 24 h following transfection. RAW cells were transfected with plasmids expressing Rab7-RILPC33-GFP (RILPC33-GFP) or wild-type Arl8b-GFP (Arl8bWT-GFP), which were previously described in (Cantalupo et al., 2001; Hofmann and Munro, 2006). The bacterial expression vector pZsGreen (Takara Bio USA, Inc., formerly Clontech Laboratories, Inc., 632446) was transformed into E. coli DH5α to generate ZsGreen-expressing bacteria.

Pharmacological treatment of cells

Apilimod (Toronto Research Chemicals, Toronto, ON) was used at 20 nM for 40 min, unless otherwise indicated, to deplete cellular PtdIns(3,5)P_2. H_2O_2 (Bio Basic, Markham, ON) was used as indicated. Rotenone, 1-chloro-2,4,-dinitrobenzene (CDNB; Sigma-Aldrich, Oakville, ON) and monocholorobimane (MCB; Sigma-Aldrich, Oakville, ON) were used as indicated to generate ROS by respectively inhibiting mitochondrial respiratory chain complex I, thioredoxin reductase and depleting glutathione. Bovine liver catalase (Sigma-Aldrich) and N-acetyl-L-cysteine (NAC) (Bio Basic) were used as anti-oxidants. Paclitaxel and nocadozole (both from Sigma-Aldrich) were used at 1 or 10 μM and 5 or 10 μM to stabilize and depolymerize microtubules, respectively. Latrunculin A (Abcam, Toronto, ON) and cytochalasin D (EMD Millipore, Toronto, ON) were used at 1 μM and 5 μM, respectively to depolymerize actin. Ikarugamycin (Sigma-Aldrich) and dyngo-4A (Abcam, Cambridge, MA) used to inhibit clathrin and dynamin respectively.

Lysosome labelling

Lysosomes were labelled by incubating cells with 200 μg/mL Alexa^{546}-conjugated dextran or with 200 μg/mL Alexa^{488}-conjugated dextran (Thermo Fisher Scientific, Mississauga, ON) or with 2.5 mg/mL Lucifer yellow (Thermo Fisher Scientific, Mississauga, ON) for 2 h in complete media at 37 ºC in 5% CO_2. Cells washed with phosphate-buffered saline (PBS) and resupplied with complete cell-specific media for 1 h to chase the fluid-phase marker to lysosomes before pharmacological manipulation and live-cell imaging. We note that we use “lysosomes” to

represent a potential mixture of late endosomes, lysosomes and endolysosomes (Bright et al., 1997; Choy et al., 2018).

Live- and fixed-cell spinning disc confocal microscopy

Microscopy and imaging were done with a Quorum DisKovery spinning disc confocal microscope system equipped with a Leica DMi8 microscope connected to an iXON 897 EMCCD camera, controlled by Quorum Wave FX powered by MetaMorph software, using 63x 1.4 NA oil-immersion objective (Quorum Technologies, Guelph, ON). Live-cell imaging was performed using environmental chamber set to 5% CO_2 and 37 ºC in complete cell-specific medium. Standard excitation and emission filter sets and lasers were used for all fluorophores. RAW and HeLa cells, unless otherwise indicated, were imaged as z-projections of 45-55 z-planes with 0.3 µm distance between each plane, or 20-30 z-planes with 0.3 µm distance between each plane for RPE cells, as acquired by spinning disc confocal microscopy. For time-lapse imaging, RAW cells were imaged using single, mid-section z-plane every 4 s for 3 min. RPE cells were imaged using single, mid-section z-plane every 8 s for 6 min. Clathrin-eGFP expressing RPE cells were imaged every 2 min for 40 min.

Detection of ROS production

For determining intracellular ROS production, we incubated RAW 264.7 macrophages with 5 µM of the cell-permeable redox sensitive dye, CellROX Green (Thermo Fisher Scientific), for 30 min at 37 ºC with 5% CO_2 in the dark during treatment with various ROS producing agents.

Cells were washed twice with PBS followed by replenishment with complete media and imaging.

Immunofluorescence and F-actin imaging

Following experimentation, cells were fixed for 15 min with 4% (v/v) paraformaldehyde in PBS, permeabilized for 10 min with 0.1% Triton X-100 (v/v) in PBS, and then blocked with 3% BSA (v/v) in PBS. Subsequently, cells were incubated with mouse monoclonal antibody against α-tubulin (1:200; Sigma-Aldrich), followed by incubation with donkey Dylight-conjugated polyclonal antibody against mouse IgG (1:1000; Bethyl), and samples were then mounted in Dako mounting media for subsequent imaging. Alternatively, lysosomes were labelled with Alexa^{488}-conjugated dextran as before, followed by fixation for 15 min with 4% (v/v) paraformaldehyde, permeabilized for 10 min with 10 μg/ml digitonin (Promega, Madison, WI), and blocked with 3% BSA (v/v), all solutions in PBS. Cells were then stained for F-actin with fluorescent-phalloidin (ThermoFisher Scientific).

Image analysis

To determine lysosome number, individual lysosome volume and total cellular lysosome volume, we used Volocity (Volocity 6.3.0) particle detection and volumetric tools. Z-stack images were imported into Volocity and a signal threshold was applied at 2x the average cytosolic fluorescence intensity. Particles were defined as being greater than 0.3 μm^3 for inclusion into the analysis, and if necessary, a watershed function was applied to split lysosome aggregates caused by thresholding. Regions of interest were drawn surrounding individual cells

for cell-to-cell analysis. Lysosome speed, track length, and displacement were assessed using Imaris (BitPlane, Concord, MA) with 'ImarisTrackLineage' module.

To determine the level of membrane-bound RILP-C33 and Arl8b, we estimated the membrane-bound to cytosolic ratio of fluorescently-tagged proteins. Using ImageJ, lines that were 3-pixel wide by 20-40-pixel long were assigned to areas of transfected cells using a predetermined grid to avoid bias but excluding the nucleus. Plot profiles were then obtained, exported into an Excel spreadsheet, values were arranged according to fluorescence intensity, and the ratio calculated for highest 10 pixels over lowest 10 pixels along the length of the line (F_H/F_L fluorescence ratio); the expectation is that values approximate to 1 represent low membrane signal due to mostly cytosolic signal, while ratio values greater than 1 represent signal that localizes to punctate structures relative to cytosol (Chintaluri et al., 2018).

For determination of clathrin-GFP on lysosomes, RPE cells stably expressing clathrin heavy chain-eGFP were loaded with Alexa^{546}-conjugated dextran and treated with apilimod, followed by imaging with spinning disc confocal microscope. Image analysis was performed using ImageJ by thresholding Alexa^{546}-conjugated dextran signal and generating a mask, which was then applied to the green (clathrin) channel to determine the GFP fluorescence intensity on regions marked by dextran signal. Regions of interest within the cytosol and the extracellular space were drawn to respectively obtain mean cytosolic fluorescence intensity and background. These values were then used to calculate the ratio of lysosome-to-cytosol clathrin-eGFP. To determine intracellular CellROX Green fluorescence or MCB-GSH adduct fluorescence emissions, images were imported onto Volocity (Volocity 6.3.0), regions of interest drawn around cell, and mean fluorescence intensity per cell recorded. Image contrast enhancement was performed with Adobe Photoshop CS (Adobe Systems, San Jose, CA) or ImageJ without

changing relative signals and applied after quantification. Adobe Illustrator CS (Adobe Systems) was used for constructing figures.

Lysosome fractionation

RAW 264.7 cells were grown and used according to manufacturer's instructions to obtain membrane fractions by differential sedimentation ultracentrifugation using a density gradient (Lysosome Isolation Kit, Sigma-Aldrich, LYSISO1). Briefly, cells were lysed and homogenates centrifuged 1,000 x*g* for 10 min at 4 ˚C to separate unbroken cells and debris from cytoplasmic membranes. The supernatant was further centrifuged at 20,000 x*g* for 20 min at 4 ˚C to pellet lysosomes and other organelles. The pellet was reconstituted with Optiprep density gradient medium (60% (w/v) solution of iodixanol in water and sucrose) and loaded onto of a step-wise sucrose gradient as described by the manufacturer and subjected to ultracentrifugation at 150,000 x*g* for 4 h at 4 ˚C using SW50.1 rotor (Beckman Coulter, Mississauga, ON). Fractions were then collected and subject to denaturation with Laemmli buffer until further use.

Western Blotting

For whole-cell lysates in 2x Laemmli buffer, cells were passed six times through 27-gauge needle, heated and proteins resolved through SDS-PAGE with 10% acrylamide resolving gel. Proteins were then transferred to a PVDF membrane, blocked and incubated with primary and HRP-conjugated secondary antibodies in Tris-buffered saline containing 5% skimmed milk and 0.1% Tween-20. Clarity enhanced chemiluminescence (Bio-Rad Laboratories, Mississauga, ON) was used to visualize proteins with ChemiDoc Touch Imaging system (Bio-Rad). Protein

quantification was performed using Image Lab software (Bio-Rad) by sequentially normalizing against a loading control and against vehicle-treated condition. Rabbit polyclonal antibodies used were against VAPB (1:3000, HPA013144, Sigma-Aldrich). Mouse monoclonal antibodies used were against clathrin heavy chain (1:500, sc-12734, Santa Cruz Biotechnology) and ATP5A (1:2000, ab14748, Abcam). Rat monoclonal antibodies were against LAMP1 (1:200, 1D4B, Developmental Studies Hybridoma Bank, Iowa City, IO). Goat polyclonal antibody used against dynamin 2 (1:1000, sc-6400, Santa Cruz Biotechnology). Secondary antibodies were raised in donkey (Bethyl) and HRP-conjugated.

Phosphoinositide labelling with ^{3}H-*myo*-inositol and HPLC-coupled flow scintillation

RAW cells were incubated for 24 h with inositol-free DMEM (MP Biomedica, CA) containing 10 μCi/ml *myo*-[2-^{3}H(N)] inositol (Perkin Elmer, MA), 1X insulin-transferrin-selenium-ethanolamine (Gibco), 10% dialyzed FBS (Gibco), 4 mM L-glutamine (Sigma-Aldrich) and 20 mM HEPES (Gibco). Cells were then treated with rotenone, H_2O_2 and/or apilimod as indicated. Cells were lysed and lipids precipitated with 600 μl of 4.5% perchloric acid (v/v) for 15 min on ice, collected by scraping and pellet obtained at 12000 x*g* for 10 min. Then, 1 ml of 0.1 M EDTA was used to wash pellets followed by resuspension in 50 μl water. This was followed by 500 μl of methanol/40% methylamine/1-butanol [45.7% methanol: 10.7% methylamine: 11.4% 1-butanol (v/v)] used for 50 min at 53 ˚C to deacylate phospholipids. Sample pellets were vaccum-dried and washed twice in 300 μl water with vaccum-drying. Deacylated phospholipids were extracted from dried sample pellets by resuspending pellet in 450 μl water and 300 μl 1-butanol/ethyl ether/ethyl formate (20:4:1), vortexing 5 min, followed by centrifugation 12000 x*g* for 2 min and then the bottom aqueous layer was collected. Extraction was performed three times

followed by vaccum-drying the aqueous layer and resuspending lipids in 50 µl water. For all treatment samples, equal ^{3}H counts were loaded and separated by HPLC (Agilent Technologies, Mississauga, ON) through 4.6 x 250-mm anion exchange column (Phenomenex, Torrance, CA) using a 1 ml/min flow rate with a gradient set with water (buffer A) and 1 M $(NH_4)_2HPO_4$, pH 3.8 (phosphoric acid adjusted) (buffer B) as follows: 0% B for 5 min, 0 to 2% B for 15 minutes, 2% B for 80 minutes, 2 to 10% B for 20 minutes, 10% B for 30 minutes, 10 to 80% B for 10 minutes, 80% B for 5 minutes, 80 to 0% B for 5 minutes. Radiolabel signal was detected with a 1:2 ratio of eluate to scintillant (LabLogic, Brandon, FL) in a β-RAM 4 (LabLogic) and analyzed by Laura 4 software. Each phosphoinositide species detected was normalized against the parent phosphatidylinositol peak as described in (Ho et al., 2016).

Phagocytosis particle preparation and phagosome maturation assays

pZsGreen-containing bacteria were grown at 37 °C in Lysogeny Broth (LB), supplemented with 1% glucose to suppress leaky ZsGreen expression, and 100 µg/mL ampicillin (LB Growth Media). To produce ZsGreen-expressing bacteria, bacteria cultures were grown overnight in liquid LB Growth Media. The bacteria culture was then subcultured 1:100 in LB supplemented with ampicillin and without glucose (LB Expression Media) and incubated at 37 °C to mid-log growth phase. Isopropylthio-β-galactoside was added into the subculture to a final concentration of 100 µM, and the subculture was incubated for another 3 hours. Bacteria were washed with PBS, then fixed with 4% PFA, and stored at 4 °C in PFA. Prior to use, fixed bacteria were washed with PBS to remove PFA.

RAW macrophages at 30 to 60% confluence were treated with 1 mM H_2O_2 or 0.1% ddH_2O (vehicle control) for 1 h. Subsequently, 8.0×10^7 bacteria (0.1 OD × 1 mL) were introduced to macrophages and centrifuged at 400 x g for 5 minutes to synchronize phagocytosis. Macrophages were incubated for 20 minutes in the presence of H_2O_2 or ddH_2O before washing with PBS and incubating in media containing H_2O_2 or ddH_2O for 40 minutes. Except for PBS wash, macrophage exposure to H_2O_2 was uninterrupted. Macrophages were washed with PBS then fixed with 4% PFA. Cells were then incubated in 1% w/v glycine to quench PFA. Cells were then blocked with 1% Bovine Serum Albumin (BSA), then external bacteria were immunolabeled with rabbit anti-*E.* coli antibodies (1:100, Bio-Rad Antibodies, 4329-4906), followed by DyLight 650-conjugated donkey anti-rabbit IgG antibodies (1:1000, Bethyl Laboratories, Inc., A120-208D5). Cells were then permeabilized with ice-cold methanol and blocked with 1% BSA. LAMP-1 lysosomal marker protein was immunolabeled with rat anti-LAMP-1 antibodies (1:100, 1D4B, Developmental Studies Hybridoma Bank, Iowa City, IO), followed by DyLight 550-conjugated donkey anti-rat IgG antibodies (1:1000, Bethyl Laboratories, Inc., A110-337D3). Coverslips were mounted with Dako Fluorescence Mounting Medium (Agilent, S302380-2) for imaging.

FIJI was used for image processing and quantitative image analysis of phagosome maturation. Internal bacteria masks were produced by applying a subtraction mask using external bacteria signal. “Noise” particles defined as being a few pixels in size were removed manually. The internal bacteria mask was converted to binary and dilated to reach the edges of the phagosomes (LAMP1 signal). LAMP-1 signal colocalized to the internal bacteria mask was analyzed cell-by-cell, and the mean LAMP-1 fluorescence intensity per cell was obtained.

Statistical analysis

All experiments were performed independently at least three times. Respective figure legends indicate number of cells/samples assessed, mean, standard error of mean (s.e.m.) and number of independent experiments. For analysing significant difference between various treatment groups, we used unpaired Student's t-test when comparing two groups only or one-way ANOVA test when comparing multiple treatment conditions in non-normalized controls. Tukey's *post hoc* test coupled to ANOVA tests was used to evaluate pairwise conditions. Statistical significance was defined as $P>0.05$. Software used for analysis was GraphPad Prism 8.

Results

Stimulation of ROS suppresses lysosome enlargement during acute PIKfyve inhibition

We previously observed that phototoxicity from extended laser excitation by spinning disc confocal fluorescence microscopy arrested lysosome enlargement during acute PIKfyve suppression (Choy et al., 2018). We speculated that this arrest may be due to ROS production caused by intense light energy (Icha et al., 2017). This led us to hypothesize that other mechanisms of ROS generation could impair lysosome enlargement during acute inhibition of PIKfyve. To test this, we exposed cells to H_2O_2, rotenone, CDNB, or MCB, which respectively cause ROS accumulation by decoupling the mitochondrial electron chain, inhibiting glutathione S-transferase, and impairing thioredoxin (Finkel, 2012; Heinz et al., 2017; Kamencic et al., 2000; Padgaonkar et al., 2015). We first demonstrated that each of these manipulations enhanced ROS levels by using CellROX Green, a redox sensitive dye whose fluorescence is proportional to

ROS levels, or by measuring fluorescence generated by MCB-glutathione adduct (Fig. S1). Remarkably, we then observed that all four ROS inducers arrested lysosome enlargement in cells treated with apilimod, a potent and selective PIKfyve blocker (Fig. 1). More specifically, RAW cells treated with apilimod alone suffered an increase in the size of individual lysosomes (Fig. 1B) and a decrease in lysosome number (Fig. 1C), indicating that lysosomes coalesced. As we documented before, the total cellular volume of the lysosome population was unchanged between resting and apilimod-treated cells (Fig. 1D). In comparison, co-exposure of cells with apilimod to either H_2O_2, rotenone, CDNB or MCB prevented lysosome enlargement and reduction in lysosome number (Fig. 1A-D). No significant changes to lysosome number, size of individual lysosomes and total lysosome volume were observed when ROS agonists were used alone (Fig. 1A-D). To determine if ROS were the active agent that blocked lysosome coalescence during apilimod-treatment for at least one of the four treatments used, we employed N-acetyl-L-cysteine (NAC) as an anti-oxidant during rotenone co-administration (Aldini et al., 2018). Indeed, cells co-exposed with apilimod, rotenone and NAC displayed larger lysosomes than cells treated with apilimod and rotenone alone (Fig. 2), indicating that ROS are the active agent arresting lysosome enlargement during PtdIns(3,5)P_2 depletion.

To ensure that these observations were not specific to murine RAW macrophages, we assessed apilimod-induced lysosome coalescence in human-derived RPE and HeLa cells co-exposed to H_2O_2 or CDNB. As with RAW cells, while apilimod-alone induced lysosome coalescence in HeLa and RPE cells, counterpart cells co-administered apilimod and H_2O_2 or CDNB strongly resisted lysosome enlargement and reduction in lysosome number (Sup. Fig. S2). As before, no changes were observed under any treatment to the total lysosomal volume within these cell types (Sup. Fig. S2D, S2H). Overall, our observations suggest that generation

of ROS via distinct mechanisms can impair lysosome coalescence caused by PIKfyve inhibition in several cell types.

ROS stimulation arrests apilimod induced lysosome enlargement without neutralizing apilimod or stimulating PtdIns(3,5)P_2 synthesis

We next considered the possibility that higher ROS load within cells may degrade the structural integrity of apilimod, relieving acute PIKfyve suppression and thus preventing lysosome coalescence. To test this, we co-incubated apilimod with H_2O_2 in complete medium *in vitro* for 40 min. Following this incubation, we added catalase to decompose H_2O_2 and then transferred the reaction mixture onto RAW macrophages to observe if apilimod was still able to induce lysosome enlargement. We found that apilimod pre-exposed to H_2O_2 was still able to increase lysosome size and decrease lysosome number similarly to an aliquot of naïve apilimod (Fig. 3A-D), suggesting that H_2O_2 did not degrade apilimod. Moreover, while H_2O_2 arrested apilimod-mediated lysosome enlargement, the co-addition of catalase to apilimod and H_2O_2 permitted lysosome enlargement, further suggesting that H_2O_2 is a direct suppressor of lysosome coalescence in PIKfyve-inhibited cells (Fig. 3A-D). Therefore, we provide additional evidence that ROS rescue lysosome coalescence during acute PIKfyve inhibition.

We next examined if ROS rescue lysosome coalescence during PIKfyve inhibition by increasing the levels of PtdIns(3,5)P_2 in cells. In part, this may occur because ROS species reversibly oxidize catalytic cysteine residues on protein and lipid phosphatases, abating their activity (Lee et al., 1998; Leslie et al., 2003; Schieber and Chandel, 2014). Therefore, augmented ROS levels may inhibit the Fig4 lipid phosphatase, counteracting PIKfyve inhibition

with apilimod and boosting PtdIns(3,5)P_2 levels (Sbrissa et al., 2007). This putative PtdIns(3,5)P_2 elevation may then be sufficient to prevent lysosome coalescence in cells exposed to apilimod and ROS. To test this hypothesis, we measured PtdInsP levels in cells treated with H_2O_2 or rotenone with and without apilimod by labelling cells with ^{3}H-*myo*-inositol and using HPLC-coupled flow scintillation (Ho et al., 2016). However, we observed a similar drop of about 80% in Ptdns(3,5)P_2 in cells treated with apilimod with or without ROS agents (Fig. 3E, F), suggesting that ROS stimulation does not significantly elevate PtdIns(3,5)P_2 levels. In addition, inhibition of PIKfyve typically causes an increase in PtdIns(3)P levels (Fig. 3E, F). While rotenone had no effect on this increase, H_2O_2 appeared to prevent this spike in PtdIns(3)P levels during apilimod treatment (Fig. 3E). The significance of this change is not clear to us but given that rotenone still increased PtdIns(3)P and prevented lysosome coalescence, it is not likely to explain our observations. Overall, ROS prevents lysosome coalescence during PIKfyve inhibition via a mechanism that is independent of PtdIns(3,5)P_2 levels. We previously showed that removal of apilimod reversed lysosome coalescence. Thus, we next tested whether ROS can accelerate lysosome fragmentation upon removal of apilimod.

ROS accelerate lysosome fragmentation during PIKfyve reactivation

Removal of apilimod elicited reversal of lysosome coalescence, re-establishing lysosome size and number after >3 h post drug removal (Choy et al., 2018). To test if ROS exposure could accelerate this reversal in lysosome coalescence, we treated RAW cells with apilimod for 1 h and then incubated cells with fresh, drug-free medium to reactivate PIKfyve with and without H_2O_2, rotenone, CDNB, or MCB during this wash duration. As before, apilimod increased lysosome size and decreased lysosome number, while chasing cells for 2 h after drug removal reversed this

phenotype partly; longer incubation ultimately reverses lysosome enlargement completely (Choy et al., 2018). Strikingly, exposure to any of the four ROS agents during the apilimod-free chase accelerated the rate of lysosome fragmentation, rapidly increasing lysosome number and reducing the size of individual lysosomes (Fig. 4A-D). ROS may prevent lysosome coalescence or accelerate lysosome fragmentation by either abating lysosome fusion rates and/or increasing fission rates, which we next sought to differentiate.

ROS alter the microtubule system

We first examined whether ROS altered the microtubule system given its role in facilitating homotypic and heterotypic lysosome fusion. In fact, we previously showed that disruption of the microtubule system and microtubule motor activity blocked lysosome coalescence during PIKfyve inhibition (Choy et al., 2018). We inspected the microtubule system in RAW macrophages (Fig. 5A) and RPE cells (Fig. 5B) exposed to the four ROS agents by immunofluorescence staining against α-tubulin. We observed that all four ROS agonists altered the microtubule system, but in distinct ways. Relative to untreated RAW macrophages or RPE cells, qualitative analysis of immunofluorescence images suggest that H_2O_2 makes microtubules more stable and extended, whereas increasing concentrations of rotenone, CDNB and MCB seemed to depolymerize microtubules, resulting in shorter microtubules and diffused staining (Fig. 5). These observations indicate that type of ROS and/or the site of ROS synthesis differentially affects microtubules, and potentially lysosome dynamics.

Disparate ROS effects on lysosome motility

To dissect these observations further, we considered that microtubule disruption would impair lysosome motility and/or lysosome fusion. To test this model, we quantified lysosome motility and the ability of lysosomes to fuse with phagosomes. First, we conducted live-cell imaging over 3 and 6 min for RAW macrophages (Fig. 6A-C, Movies 1-6) and RPE cells (Fig. 6D-F, Movies 7-13), respectively, treated with vehicle or ROS agents. Using these videos, we then extracted lysosome speed, track length, and vectorial displacement as indicators of lysosome motility. To our surprise, H_2O_2 was the only ROS agent that reduced lysosome speed, track length and vectorial displacement in RAW and in RPE cells, with the strongest effect on the latter cell type (Fig. 6). To understand whether microtubule stability was sufficient to impair lysosome coalescence or affect lysosome motility, we performed a control experiment by treating RAW cells with paclitaxel, a microtubule stabilizing agent (Weaver, 2014). However, paclitaxel did not impair lysosome coalescence caused by apilimod and may actually enhance lysosome motility indicators (Sup. Fig. S3A-G, Movies 14-16), suggesting that H_2O_2 blocks apilimod-mediated lysosome enlargement via a distinct mechanism, perhaps by displacing motors from lysosomes or impairing motor activity. If so, this does not seem to occur by reducing the levels of GTP-Rab7 or Arl8b GTPase loaded onto lysosomes (Sup. Fig. S4).

Given impaired lysosome motility caused by H_2O_2, we next sought to determine if H_2O_2 impaired also lysosome fusogenecity by using phagosome-lysosome fusion as a model. RAW cells were treated with H_2O_2 or vehicle for 1 h, followed by phagocytosis of bacteria for 20 min and a chase period of 40 min to permit phagosome maturation. The degree of phagosome-lysosome fusion was assessed by quantifying the amount of LAMP-1 fluorescent signal present on bacteria-containing phagosomes. We observed that H_2O_2-treated RAW cells had less LAMP-1 fluorescence signal localized to bacteria-containing phagosomes compared to vehicle-treated

RAW macrophages (Fig. 7). This suggests that H_2O_2 impaired the ability of lysosomes to fuse with target organelles, consistent with reduced lysosome motility. Overall, we suggest that H_2O_2 can prevent lysosome coalescence during PIKfyve inhibition by impairing lysosome motility and probability of fusion with other organelles, including phagosomes and other lysosomes.

In comparison to H_2O_2, rotenone, MCB and CDNB did not impair measures of lysosome motility in RAW macrophages or RPE cells (Fig. 6A-C) at concentrations sufficient to block apilimod-induced lysosome coalescence. Interestingly, nocadozole strongly impaired all measures in RPE cells but had mild effects on RAW cells (Fig. 6). This is likely because RAW macrophages depolymerized for microtubules appeared to become rounder and taller, causing a wobbling motion that moved lysosomes in bulk (See Supplemental Movies 1-6). In comparison, RPE cells were flatter and more resistant to this oscillating effect (See Supplemental Movies 7-13). Given that nocodazole in RPE cells hindered lysosome motility, but CDNB, MCB and rotenone had no effect on lysosome motility measures in RPE cells, this suggests that rotenone, CDNB and MCB only partially disrupt the microtubule system. Thus, the extent of microtubule depolymerization caused by rotenone, CDNB and MCB is not sufficient to explain how these agents prevent lysosome enlargement during apilimod treatment. We next examined if ROS species can also alter mechanisms associated with lysosome fission.

Clathrin and dynamin are not required for ROS-induced lysosome fragmentation

Lysosomes and related organelles such as autolysosomes can assemble fission machinery, including the canonical fission components, clathrin and dynamin (Boutry et al., 2018; Rong et al., 2012; Saffi and Botelho, 2019; Traub et al., 1996). We sought to determine if ROS species

like H_2O_2 stimulate clathrin and dynamin-2 to boost fission and prevent lysosome coalescence during PIKfyve inhibition. First, we observed no changes in the levels of lysosome-associated clathrin-eGFP in vehicle or apilimod-treated RPE cells. In comparison, clathrin-eGFP was recruited at higher levels to lysosomes labelled with Alexa^{546}-conjugated dextran after H_2O_2 treatment in both the presence or absence of apilimod (Sup. Fig. S5A, B). To complement our observations, we treated RAW 264.7 cells with vehicle or H_2O_2, followed by sucrose gradient ultracentrifugation to fractionate organelles and probed for clathrin and dynamin by Western blotting. Strikingly, we saw a consistent increase in the level of clathrin and dynamin-2 to LAMP1-positive lysosome fractions in cells treated with H_2O_2 relative to resting cells (Sup. Fig. S5C-E). To test whether this enhanced recruitment of clathrin and dynamin aided in lysosome fragmentation during PIKfyve reactivation in the presence of H_2O_2, we inhibited clathrin and dynamin with ikarugamycin and dyngo 4a, respectively (Elkin et al., 2016; McCluskey et al., 2013). Nevertheless, there was no significant difference in the H_2O_2-mediated rescue of lysosome coalescence during PIKfyve reactivation when clathrin or dynamin were arrested (Fig. 8, Sup. Fig. S6). Similarly, there was no difference in lysosome fragmentation during rotenone exposure when cells were incubated with dyngo 4a (Sup. Fig. S6). Overall, while at least H_2O_2 seems to recruit clathrin and dynamin to lysosomes (and perhaps other membranes), our data do not support a role for clathrin and dynamin in preventing lysosome coalescence during PIKfyve inhibition under the used conditions.

ROS can rescue lysosome coalescence by actin depolymerization

There is growing evidence that F-actin-based structures may regulate endosomal and lysosomal fission, either through the action of acto-myosin constriction or the assembly of fission

machinery that remains to be fully defined (Hong et al., 2015; Hoyer et al., 2018; Saffi and Botelho, 2019). In fact, work by Hong et al. suggests that PIKfyve inhibition causes branched actin accumulation on endosomes (likely including lysosomes based on their markers) (Hong et al., 2015). We set to understand if at least some ROS can rescue lysosome coalescence during PIKfyve inhibition by reversing these F-actin assemblies on lysosomes by co-staining with fluorescent phalloidin. Indeed, PtdIns(3,5)P_2 depletion increased the number of F-actin puncta associated with lysosomes (Fig. 9A, B), as previously reported (Bissig et al., 2019; Hasegawa et al., 2016). Interestingly, co-administration of rotenone or CDNB with apilimod reduced F-actin puncta associated with lysosomes (Fig. 9A, B). These observations indicate that ROS generated by rotenone and CDNB help prevent or reverse lysosome coalescence during PIKfyve inhibition by boosting actin turnover on lysosomes.

To further test whether actin depolymerization helps prevent lysosome coalescence during PIKfyve inhibition and accelerate lysosome fragmentation during PIKfyve inhibition, we compared lysosome volumetrics in cells treated with the actin depolymerizing agents, cytochalasin B or latrunculin A. Strikingly, we found that cytochalasin B and latrunculin A treatments both impaired lysosome coalescence during apilimod treatment, as well as accelerated lysosome fragmentation after apilimod removal and PIKfyve reactivation (Fig. 9C-F). Collectively, our observations suggest that at least certain types of ROS prevent lysosome coalescence during acute PIKfyve inhibition by alleviating F-actin amassed on lysosomes, likely facilitating fission.

Discussion

Low PtdIns(3,5)P_2 levels causes multiple defects including impaired autophagic flux, nutrient recycling, and phagosome resolution (McCartney et al., 2014; Saffi and Botelho, 2019). These defects are likely derived from the inability of lysosomes to reform or separate after fusion with other lysosomes, late endosomes, phagosomes, and autolysosomes (Bissig et al., 2017; Choy et al., 2018; Gan et al., 2019; Krajcovic et al., 2013; Saffi and Botelho, 2019). As a corollary, lysosomes coalesce to become larger but fewer (Bissig et al., 2017; Choy et al., 2018). Thus, identification of mechanisms or compounds that can drive lysosome fission may prove useful to rescue autophagic flux, degradative capacity, and lysosome dynamics in cells exhibiting reduced PtdIns(3,5)P_2 levels. Such mechanisms or compounds may act to up-regulate PtdIns(3,5)P_2 levels in conditions of insufficient PIKfyve activity like those caused by mutations in the Fig4 lipid phosphatase (Chow et al., 2007). For example, the cyclin/cyclin-dependent kinase, Pho80/Pho85, phosphorylates Fab1 to upregulate the levels of PtdIns(3,5)P_2 in response to hypertonic shock, protecting yeast cells from osmotic shock (Cooke et al., 1998; Jin et al., 2017). Alternatively, activating mechanisms downstream of PtdIns(3,5)P_2 that enable lysosome fission directly may also rescue lysosome dynamics.

We previously observed that photo-toxicity during live-cell imaging with spinning disc confocal microscopy prevented lysosome coalescence during apilimod-mediated PIKfyve inhibition (Choy et al., 2018). While unfortunately blunting our ability to perform high spatio-temporal resolution of lysosome enlargement by live-cell imaging, we questioned if other sources of ROS could also prevent lysosome coalescence during PIKfyve inhibition. Indeed, we provide evidence here that ROS generated by diverse approaches can counteract and even reverse lysosome coalescence during PIKfyve inhibition. Notably, neither H_2O_2 or rotenone rescued lysosome size by up-regulating the levels of PtdIns(3,5)P_2. This suggests that ROS

counteract lysosome coalescence by acting downstream of PtdIns(3,5)P_2, or by stimulating parallel processes that promote lysosome fission or impair lysosome fusion. Our work suggests that the exact mechanism may depend on the ROS type and/or mode of production and/or location since H_2O_2 had distinct effects from those by CDNB, MCB and rotenone.

We previously showed that disrupting the microtubule system with nocodazole or impairing motor proteins abated lysosome coalescence during PIKfyve inhibition (Choy et al., 2018). Thus, we explored whether ROS agents disrupted lysosome motility, which would impair fusogenicity. We observed that only H_2O_2 significantly arrested lysosome motility and reduced fusogenicity. In addition, we also saw a more defined microtubule network in H_2O_2-treated cells, suggesting that microtubules were stabilized by H_2O_2. Whether this effect is generalizable is debatable since there are contradictory observations about the effect of H_2O_2 on the microtubule system, which may depend on cell type and experimental conditions employed (Debattisti et al., 2017; Mackeh et al., 2014; Valen et al., 1999). Regardless, microtubule stabilization is not sufficient to impair lysosome motility since paclitaxel did not prevent lysosome enlargement caused by apilimod or impair lysosome motility. Thus, we propose that H_2O_2 impairs lysosome motility by disrupting motor activity, and/or impairing motor interactions with lysosomes and/or microtubules. Mitochondria may offer some insight since their motility was also arrested by H_2O_2 (Debattisti et al., 2017). H_2O_2 stimulated p38α MAPK, which then interrupted motor adaptor complex function. Motors themselves retained their activity since forced anchorage of kinesin to mitochondria maintained mitochondrial motility in the presence of H_2O_2 (Debattisti et al., 2017). Thus, H_2O_2 may disrupt kinesin and/or dynein adaptors like RILP-ORP1L-dynein or SKIP-kinesin, though our work suggests that this is not likely occurring by altering GTP-Rab7 and Arl8b loading onto lysosomes.

In comparison to H_2O_2, ROS produced by mitochondrial uncoupling (rotenone) or amassed by disrupting catalase and thioredoxin (MCB and CDNB) partially depolymerized the microtubule system under the employed conditions, though perplexingly all three treatments had minor effects on lysosome motility. While for RAW cells, this may be due to a whole-cell wobble effect, RPE cells clearly show that these treatments did not affect lysosome motility, unlike H_2O_2 and nocodazole. Instead, rotenone and CDNB may prevent overt lysosome coalescence by releasing a dense F-actin network that assembles on lysosomes during PIKfyve inhibition; we did not test the effects of MCB in this study. Consistent with this, actin depolymerizers also reduced lysosome coalescence during acute PIKfyve inhibition and accelerated lysosome fragmentation during PIKfyve reactivation. These observations may be consistent with those by Hong *et al.*, wherein PtdIns(3,5)P_2 modulates branched actin dynamics on endosomes (markers apply to lysosomes as well) by regulating cortactin (Hong et al., 2015). The authors showed that PIKfyve inhibition increased actin density on endo/lysosomes, which consequently impaired fission and caused enlargement (Hong et al., 2015). Additionally, PIKfyve was recently shown to modulate branched F-actin to help drive melanosome maturation (Bissig et al., 2019). Indeed, branched F-actin has emerged as a major player in membrane fission for endo/lysosomes nucleated by ER-endo/lysosomes contact sites (Friedman et al., 2013; Rowland et al., 2014). Thus, our work suggests that ROS generated by rotenone, CDNB, and perhaps MCB, may abate lysosome coalescence by relieving dense F-actin networks that form on lysosomes during PIKfyve inhibition.

While oxidative stress in cells can hinder lysosome coalescence during PIKfyve inhibition and accelerate lysosome fragmentation during PIKfyve reactivation, the exact mechanisms of action depends on the type of ROS and/or mode of production. For H_2O_2, we

speculate that this may be the direct agent that alters microtubule-motor dynamics, or alternatively, it is its breakdown product, the $OH^{\cdot}$ radical that causes the observed changes (Korge et al., 2015; Nordberg et al., 1998; Ochi et al., 2016). In comparison, rotenone, CDNB and MCB may act by producing O_2^-, which may increase turnover of the lysosomal F-actin network to shift lysosome dynamics towards fission. It should be noted that while MCB interacts with GSH and prevents H_2O_2 decomposition by glutathione peroxidase, MCB can also interact with thiol residues of other enzymes such as thioredoxin reductase, leading to increased O_2^- production (Kamencic et al., 2000; Lubos et al., 2011; Nordberg et al., 1998). Thus, future work will need to delineate the type of ROS and their exact target that alter lysosome dynamics. Moreover, since ROS can serve as physiological signals (Brown and Griendling, 2009; Schieber and Chandel, 2014), it is tempting to suggest that particular ROS may play a role in coordinating localized processes like membrane fusion, motor activity, and membrane fission. This process or the sensors engaged by ROS may represent approaches to rescue lysosome dynamics in conditions of PtdIns(3,5)P_2 insufficiency.

References

Aguet, F., Antonescu, C. N., Mettlen, M., Schmid, S. L. and Danuser, G. (2013). Advances in analysis of low signal-to-noise images link dynamin and AP2 to the functions of an endocytic checkpoint. *Dev. Cell* **26**, 279–291.

Aldini, G., Altomare, A., Baron, G., Vistoli, G., Carini, M., Borsani, L. and Sergio, F. (2018). N-Acetylcysteine as an antioxidant and disulphide breaking agent: the reasons why. *Free Radic. Res.* **52**, 751–762.

Bissig, C., Hurbain, I., Raposo, G. and van Niel, G. (2017). PIKfyve activity regulates reformation of terminal storage lysosomes from endolysosomes. *Traffic* **18**, 747–757.

Bissig, C., Croisé, P., Heiligenstein, X., Hurbain, I., Lenk, G. M., Kaufman, E., Sannerud, R., Annaert, W., Meisler, M. H., Weisman, L. S., et al. (2019). PIKfyve complex regulates early melanosome homeostasis required for physiological amyloid formation. *J. Cell Sci.* jcs.229500.

Boutry, M., Branchu, J., Lustremant, C., Pujol, C., Pernelle, J., Matusiak, R., Seyer, A., Poirel, M., Chu-Van, E., Pierga, A., et al. (2018). Inhibition of Lysosome Membrane Recycling Causes Accumulation of Gangliosides that Contribute to Neurodegeneration. *Cell Rep.* **23**, 3813–3826.

Bright, N. A., Reaves, B. J., Mullock, B. M. and Luzio, J. P. (1997). Dense core lysosomes can fuse with late endosomes and are re-formed from the resultant hybrid organelles. *J. Cell Sci.* **110 (Pt 1**, 2027–40.

Bright, N. A., Gratian, M. J. and Luzio, J. P. (2005). Endocytic Delivery to Lysosomes Mediated by Concurrent Fusion and Kissing Events in Living Cells. *Curr. Biol.* **15**, 360–365.

Bright, N. A., Davis, L. J. and Luzio, J. P. (2016). Endolysosomes Are the Principal Intracellular Sites of Acid Hydrolase Activity. *Curr. Biol.* **26**, 2233–2245.

Brown, D. I. and Griendling, K. K. (2009). Nox proteins in signal transduction. *Free Radic. Biol. Med.* **47**, 1239–1253.

Cantalupo, G., Alifano, P., Roberti, V., Bruni, C. B. and Bucci, C. (2001). Rab-interacting lysosomal protein (RILP): the Rab7 effector required for transport to lysosomes. *EMBO J.* **20**, 683–93.

Cao, Q., Zhong, X. Z., Zou, Y., Murrell-Lagnado, R., Zhu, M. X. and Dong, X.-P. (2015). Calcium release through P2X4 activates calmodulin to promote endolysosomal membrane fusion. *J. Cell Biol.* **209**, 879–94.

Cao, Q., Yang, Y., Zhong, X. Z. and Dong, X.-P. (2017). The lysosomal Ca2+ release channel TRPML1 regulates lysosome size by activating calmodulin. *J. Biol. Chem.* **292**, 8424–8435.

Chen, Y., Azad, M. B. and Gibson, S. B. (2009). Superoxide is the major reactive oxygen species regulating autophagy. *Cell Death Differ.* **16**, 1040–1052.

Chintaluri, K., Goulden, B. D., Clemenza, C., Saffi, G., Miraglia, E., Hammond, G. R. V. and Botelho, R. J. (2018). Correction: The PH domain from the Toxoplasma gondii PH-containing protein-1 (TgPH1) serves as an ectopic reporter of phosphatidylinositol 3-phosphate in mammalian cells. *PLoS One* **13**, e0201800.

Chow, C. Y., Zhang, Y., Dowling, J. J., Jin, N., Adamska, M., Shiga, K., Szigeti, K., Shy, M. E., Li, J., Zhang, X., et al. (2007). Mutation of FIG4 causes neurodegeneration in the pale tremor mouse and patients with CMT4J. *Nature* **448**, 68–72.

Choy, C. H., Saffi, G., Gray, M. A., Wallace, C., Dayam, R. M., Ou, Z.-Y. A., Lenk, G., Puertollano, R., Watkins, S. C. and Botelho, R. J. (2018). Lysosome enlargement during inhibition of the lipid kinase PIKfyve proceeds through lysosome coalescence. *J. Cell Sci.* **131**, jcs213587.

Cooke, F. T., Dove, S. K., McEwen, R. K., Painter, G., Holmes, a B., Hall, M. N., Michell, R. H. and Parker, P. J. (1998). The stress-activated phosphatidylinositol 3-phosphate 5-kinase Fab1p is essential for vacuole function in S. cerevisiae. *Curr. Biol.* **8**, 1219–22.

Debattisti, V., Gerencser, A. A., Saotome, M., Das, S. and Hajnóczky, G. (2017). ROS Control Mitochondrial Motility through p38 and the Motor Adaptor Miro/Trak. *Cell Rep.* **21**, 1667–1680.

Dizdaroglu, M. and Jaruga, P. (2012). Mechanisms of free radical-induced damage to DNA. *Free Radic. Res.* **46**, 382–419.

Duclos, S. (2003). Remodeling of endosomes during lysosome biogenesis involves `kiss and run' fusion events regulated by rab5. *J. Cell Sci.* **116**, 907–918.

Elkin, S. R., Oswald, N. W., Reed, D. K., Mettlen, M., MacMillan, J. B. and Schmid, S. L. (2016). Ikarugamycin: A Natural Product Inhibitor of Clathrin-Mediated Endocytosis. *Traffic* **17**, 1139–1149.

Fang, X., Zhou, J., Liu, W., Duan, X., Gala, U., Sandoval, H., Jaiswal, M. and Tong, C. (2016). Dynamin Regulates Autophagy by Modulating Lysosomal Function. *J. Genet. Genomics* **43**, 77–86.

Finkel, T. (2012). From sulfenylation to sulfhydration: What a thiolate needs to tolerate. *Sci. Signal.* **5**, pe10–pe10.

Friedman, J. R., DiBenedetto, J. R., West, M., Rowland, A. A. and Voeltz, G. K. (2013). Endoplasmic reticulum–endosome contact increases as endosomes traffic and mature. *Mol. Biol. Cell* **24**, 1030–1040.

Gan, Q., Wang, X., Zhang, Q., Yin, Q., Jian, Y., Liu, Y., Xuan, N., Li, J., Zhou, J., Liu, K., et al. (2019). The amino acid transporter SLC-36.1 cooperates with PtdIns3P 5-kinase to control phagocytic lysosome reformation. *J. Cell Biol.* jcb.201901074.

Gopaldass, N., Fauvet, B., Lashuel, H., Roux, A. and Mayer, A. (2017). Membrane scission driven by the PROPPIN Atg18. *EMBO J.* **36**, e201796859.

Hasegawa, J., Iwamoto, R., Otomo, T., Nezu, A., Hamasaki, M. and Yoshimori, T. (2016). Autophagosome-lysosome fusion in neurons requires INPP5E, a protein associated with Joubert syndrome. *EMBO J.* **35**, 1853–67.

Heinz, S., Freyberger, A., Lawrenz, B., Schladt, L., Schmuck, G. and Ellinger-Ziegelbauer, H. (2017). Mechanistic Investigations of the Mitochondrial Complex I Inhibitor Rotenone in the Context of Pharmacological and Safety Evaluation. *Sci. Rep.* **7**, 45465.

Ho, C. Y., Choy, C. H. and Botelho, R. J. (2016). Radiolabeling and Quantification of Cellular Levels of Phosphoinositides by High Performance Liquid Chromatography-coupled Flow Scintillation. *J. Vis. Exp.* e53529.

Hofmann, I. and Munro, S. (2006). An N-terminally acetylated Arf-like GTPase is localised to lysosomes and affects their motility. *J. Cell Sci.* **119**, 1494–503.

Hong, N. H., Qi, A. and Weaver, A. M. (2015). PI(3,5)P2 controls endosomal branched actin

dynamics by regulating cortactin–actin interactions. *J. Cell Biol.* **210**, 753–769.

Hoyer, M. J., Chitwood, P. J., Ebmeier, C. C., Striepen, J. F., Qi, R. Z., Old, W. M. and Voeltz Correspondence, G. K. (2018). A Novel Class of ER Membrane Proteins Regulates ER-Associated Endosome Fission. *Cell* **175**, 254–265.

Icha, J., Weber, M., Waters, J. C. and Norden, C. (2017). Phototoxicity in live fluorescence microscopy, and how to avoid it. *BioEssays* **39**, 1700003.

Jin, N., Jin, Y. and Weisman, L. S. (2017). Early protection to stress mediated by CDK-dependent PI3,5P2 signaling from the vacuole/lysosome. *J. Cell Biol.* **216**, 2075–2090.

Kamencic, H., Lyon, A., Paterson, P. G. and Juurlink, B. H. J. (2000). Monochlorobimane Fluorometric Method to Measure Tissue Glutathione. *Anal. Biochem.* **286**, 35–37.

Khatter, D., Sindhwani, A. and Sharma, M. (2015). Arf-like GTPase Arl8: Moving from the periphery to the center of lysosomal biology. *Cell. Logist.* **5**, e1086501.

Korge, P., Calmettes, G. and Weiss, J. N. (2015). Increased reactive oxygen species production during reductive stress: The roles of mitochondrial glutathione and thioredoxin reductases. *Biochim. Biophys. Acta* **1847**, 514–25.

Krajcovic, M., Krishna, S., Akkari, L., Joyce, J. A. and Overholtzer, M. (2013). mTOR regulates phagosome and entotic vacuole fission. *Mol. Biol. Cell* **24**, 3736–3745.

Lee, S. R., Kwon, K. S., Kim, S. R. and Rhee, S. G. (1998). Reversible inactivation of protein-tyrosine phosphatase 1B in A431 cells stimulated with epidermal growth factor. *J. Biol. Chem.* **273**, 15366–72.

Leslie, N. R., Bennett, D., Lindsay, Y. E., Stewart, H., Gray, A. and Downes, C. P. (2003). Redox regulation of PI 3-kinase signalling via inactivation of PTEN. *EMBO J.* **22**, 5501–10.

Li, R.-J., Xu, J., Fu, C., Zhang, J., Zheng, Y. G., Jia, H. and Liu, J. O. (2016). Regulation of mTORC1 by lysosomal calcium and calmodulin. *Elife* **5**,.

Lubos, E., Loscalzo, J. and Handy, D. E. (2011). Glutathione peroxidase-1 in health and disease: from molecular mechanisms to therapeutic opportunities. *Antioxid. Redox Signal.* **15**, 1957–97.

Luzio, J. P., Rous, B. A., Bright, N. A., Pryor, P. R., Mullock, B. M. and Piper, R. C. (2000). Lysosome-endosome fusion and lysosome biogenesis. *J. Cell Sci.* **113 (Pt 9**, 1515–24.

Luzio, J. P., Pryor, P. R. and Bright, N. A. (2007). Lysosomes: fusion and function. *Nat. Rev. Mol. Cell Biol.* **8**, 622–32.

Luzio, J. P., Parkinson, M. D. J., Gray, S. R. and Bright, N. A. (2009). The delivery of endocytosed cargo to lysosomes. *Biochem. Soc. Trans.* **37**, 1019–1021.

Mackeh, R., Lorin, S., Ratier, A., Mejdoubi-Charef, N., Baillet, A., Bruneel, A., Hamaï, A., Codogno, P., Poüs, C. and Perdiz, D. (2014). Reactive oxygen species, amp-Activated protein kinase, and the transcription cofactor p300 regulate α-Tubulin acetyltransferase-1 (αtat-1/mec-17)-Dependent microtubule hyperacetylation during cell stress. *J. Biol. Chem.* **289**, 11816–11828.

Marengo, B., Nitti, M., Furfaro, A. L., Colla, R., Ciucis, C. De, Marinari, U. M., Pronzato, M. A., Traverso, N. and Domenicotti, C. (2016). Redox Homeostasis and Cellular Antioxidant Systems: Crucial Players in Cancer Growth and Therapy. *Oxid. Med. Cell. Longev.* **2016**, 6235641.

McCartney, A. J., Zhang, Y. and Weisman, L. S. (2014). Phosphatidylinositol 3,5-bisphosphate: low abundance, high significance. *Bioessays* **36**, 52–64.

McCluskey, A., Daniel, J. A., Hadzic, G., Chau, N., Clayton, E. L., Mariana, A., Whiting, A., Gorgani, N. N., Lloyd, J., Quan, A., et al. (2013). Building a Better Dynasore: The Dyngo Compounds Potently Inhibit Dynamin and Endocytosis. *Traffic* **14**, 1272–1289.

Nordberg, J., Zhong, L., Holmgren, A. and Arnér, E. S. (1998). Mammalian thioredoxin reductase is irreversibly inhibited by dinitrohalobenzenes by alkylation of both the redox active selenocysteine and its neighboring cysteine residue. *J. Biol. Chem.* **273**, 10835–42.

Ochi, R., Dhagia, V., Lakhkar, A., Patel, D., Wolin, M. S. and Gupte, S. A. (2016). Rotenone-stimulated superoxide release from mitochondrial complex I acutely augments L-type Ca^{2+} current in A7r5 aortic smooth muscle cells. *Am. J. Physiol. Circ. Physiol.* **310**, H1118–H1128.

Padgaonkar, V. A., Leverenz, V. R., Bhat, A. V, Pelliccia, S. E. and Giblin, F. J. (2015). Thioredoxin reductase activity may be more important than GSH level in protecting human lens epithelial cells against UVA light. *Photochem. Photobiol.* **91**, 387–96.

Pankiv, S., Alemu, E. a., Brech, A., Bruun, J.-A. A., Lamark, T., Øvervatn, A., Bjørkøy, G., Johansen, T., Overvatn, A., Bjørkøy, G., et al. (2010). FYCO1 is a Rab7 effector that binds to LC3 and PI3P to mediate microtubule plus end - Directed vesicle transport. *J. Cell Biol.* **188**, 253–269.

Pu, J., Guardia, C. M., Keren-Kaplan, T. and Bonifacino, J. S. (2016). Mechanisms and functions of lysosome positioning.

Renvoisé, B., Chang, J., Singh, R., Yonekawa, S., FitzGibbon, E. J., Mankodi, A., Vanderver, A., Schindler, A. B., Toro, C., Gahl, W. A., et al. (2014). Lysosomal abnormalities in hereditary spastic paraplegia types SPG15 and SPG11. *Ann. Clin. Transl. Neurol.* **1**, 379–389.

Ristow, M. and Schmeisser, S. (2011). Extending life span by increasing oxidative stress. *Free Radic. Biol. Med.* **51**, 327–336.

Rong, Y., Liu, M., Ma, L., Du, W., Zhang, H., Tian, Y., Cao, Z., Li, Y., Ren, H., Zhang, C., et al. (2012). Clathrin and phosphatidylinositol-4,5-bisphosphate regulate autophagic lysosome reformation. *Nat. Cell Biol.* **14**, 924–34.

Rosa-Ferreira, C. and Munro, S. (2011). Arl8 and SKIP Act Together to Link Lysosomes to Kinesin-1. *Dev. Cell* **21**, 1171–1178.

Rowland, A. A., Chitwood, P. J., Phillips, M. J. and Voeltz, G. K. (2014). ER Contact Sites Define the Position and Timing of Endosome Fission. *Cell* **159**, 1027–1041.

Saffi, G. T. and Botelho, R. J. (2019). Lysosome Fission: Planning for an Exit. *Trends Cell*

Biol.

Sbrissa, D., Ikonomov, O. C., Fu, Z., Ijuin, T., Gruenberg, J., Takenawa, T. and Shisheva, A. (2007). Core protein machinery for mammalian phosphatidylinositol 3,5-bisphosphate synthesis and turnover that regulates the progression of endosomal transport: Novel Sac phosphatase joins the ArPIKfyve-PIKfyve complex. *J. Biol. Chem.* **282**, 23878–23891.

Schieber, M. and Chandel, N. S. (2014). ROS function in redox signaling and oxidative stress. *Curr. Biol.* **24**, R453–R462.

Shisheva, A., Sbrissa, D. and Ikonomov, O. (2015). Plentiful PtdIns5P from scanty PtdIns(3,5)P $_2$ or from ample PtdIns? PIKfyve-dependent models: Evidence and speculation (response to: DOI 10.1002/bies.201300012). *BioEssays* **37**, 267–277.

Traub, L. M., Bannykh, S. I., Rodel, J. E., Aridor, M., Balch, W. E. and Kornfeld, S. (1996). AP-2-containing clathrin coats assemble on mature lysosomes. *J. Cell Biol.* **135**, 1801–14.

Valen, G., Sondén, A., Vaage, J., Malm, E. and Kjellström, B. T. (1999). Hydrogen peroxide induces endothelial cell atypia and cytoskeleton depolymerization. *Free Radic. Biol. Med.* **26**, 1480–1488.

Wang, T., Ming, Z., Xiaochun, W. and Hong, W. (2011). Rab7: Role of its protein interaction cascades in endo-lysosomal traffic. *Cell. Signal.* **23**, 516–521.

Ward, D. M., Leslie, J. D. and Kaplan, J. (1997). Homotypic lysosome fusion in macrophages: Analysis using an in vitro assay. *J. Cell Biol.* **139**, 665–673.

Weaver, B. A. (2014). How Taxol/paclitaxel kills cancer cells. *Mol. Biol. Cell* **25**, 2677–81.

Yang, Y., Xu, M., Zhu, X., Yao, J., Shen, B. and Dong, X.-P. (2019). Lysosomal Ca2+ release channel TRPML1 regulates lysosome size by promoting mTORC1 activity. *Eur. J. Cell Biol.* **98**, 116–123.

Zhang, X., Cheng, X., Yu, L., Yang, J., Calvo, R., Patnaik, S., Hu, X., Gao, Q., Yang, M., Lawas, M., et al. (2016). MCOLN1 is a ROS sensor in lysosomes that regulates autophagy. *Nat. Commun.* **7**, 12109.

Figure legends

Figure 1. ROS agonists prevent lysosome enlargement during acute PIKfyve suppression.

A: RAW cells pre-labelled with Lucifer yellow and exposed to vehicle or 20 nM apilimod for 40 min. These conditions were then supplemented with additional vehicle or 1 mM H_2O_2 for 40 min, 1 µM rotenone for 60 min, 10 µM CDNB for 30 min, or 5 µM MCB for 30 min.

Fluorescence micrographs are represented as z-projections of 45-55 z-plane images obtained by spinning disc microscopy. Scale bar: 5 µm. *B-D*: Quantification of individual lysosome volume (B), lysosome number per cell (C), and total lysosome volume per cell (D). Data represent mean ± S.E.M. from three independent experiments, with 25-30 cells assessed per treatment condition per experiment. One-way ANOVA and Tukey's *post-hoc* test was used, where * indicates statistical significance between indicated conditions ($p<0.05$).

Figure 2. ROS scavengers permit lysosome coalescence during acute PIKfyve suppression. *A:* RAW cells pre-labelled with Lucifer yellow and exposed to vehicle, or 0.5 µM rotenone 60 min, or 10 mM N-acetyl-L-cysteine (NAC) 120 min alone, or in presence of 20 nM apilimod for the last 40 min. Fluorescence micrographs are represented as z-projections of 45-55 z-plane images obtained by spinning disc microscopy. Scale bar: 5 µm. *B-D*: Quantification of individual lysosome volume (B), lysosome number per cell (C), and total lysosome volume per cell (D). Data represent mean ± S.E.M. from three independent experiments, with 25-30 cells assessed per treatment condition per experiment. One-way ANOVA and Tukey's *post-hoc* test was used, where * indicates statistical significance between indicated conditions ($p<0.05$).

Figure 3: Apilimod integrity and PtdIns(3,5)P_2 levels are not altered by ROS. (A) RAW cells pre-labelled with Lucifer yellow. Following reactions were performed in complete media in vitro for designated time, prior to adding to cells for an additional 40 min: vehicle; 1 mM H_2O_2 40 min; 20 nM apilimod 40 min; 20 nM apilimod preincubated with 1 mM H_2O_2 for 40 min; 20 nM apilimod preincubated with 0.5 mg/L catalase for 60 min; 1 mM H_2O_2 exposed to 0.5 mg/L

catalase for 60 min to neutralize H_2O_2, followed by 20 nM apilimod 40 min; or 20 nM apilimod exposed to 1 mM H_2O_2 for 40 min to test whether H_2O_2 degraded apilimod, followed by 0.5 mg/L catalase for 60 min to degrade H_2O_2. Fluorescence micrographs are spinning disc microscopy images with 45-55 z-planes represented as z-projections. Scale bar: 5 µm. (B-D) Quantification of individual lysosome volume (B), lysosome number per cell (C), and total lysosome volume per cell (D). AP (apilimod), CAT (catalase). Data are shown as mean $\pm$ s.e.m. from three independent experiments, with 25-30 cell assessed per treatment condition per experiment. One-way ANOVA and Tukey's *post-hoc* test used for B-D; * indicates statistical difference against control condition (P<0.05). (E-F) ^{3}H-*myo*-inositol incorporation followed by HPLC-coupled flow scintillation used to determine PtdIns(3)P and PtdIns(3,5)P_2 levels from RAW cells exposed to vehicle alone, or 1 mM H_2O_2 40 min (E), or 1 µM rotenone 60 min (F), in presence or absence of 20 nM apilimod. Data represent $\pm$ s.d. from three independent experiments. One-way ANOVA and Tukey's *post-hoc* test used for E-F; * indicates statistical difference against control condition (P<0.05).

Figure 4. ROS accelerate recovery of lysosome size and number upon PIKfyve reactivation. (A) Top two rows: RAW cells pre-labelled with Lucifer yellow were exposed to either vehicle, 1 mM H_2O_2 40 min, 1 µM rotenone 60 min, 10 µM CDNB 30 min, or 5 µM MCB 30 min. Bottom two rows: alternatively, RAW cells were first treated with 20 nM apilimod for 60 min (0 h), followed by apilimod removal and replenishment with complete media for 2 h in the presence of vehicle, H_2O_2, rotenone, CDNB, or MCB at previously indicated concentrations. Fluorescence micrographs are spinning disc microscopy images with 45-55 z-planes represented as z-projections. Scale bar: 5 µm. (B-D) Quantification of individual lysosome volume (B), lysosome

number per cell (C), and total lysosome volume per cell (D). Data are represented as mean ± s.e.m. from three independent experiments, with 25-30 cell assessed per treatment condition per experiment. One-way ANOVA and Tukey's *post-hoc* test used for B-D, where * indicates statistical significant difference between control conditions (P<0.05).

Figure 5. ROS agents differentially affect the microtubule system. Representative single z-focal plane immunofluorescence micrographs of RAW cells (A) or RPE cells (B) treated with vehicle, H_2O_2, rotenone, CDNB or MCB at previously used time periods and at the indicated concentrations. After treatment with ROS agents, cells were fixed and immunostained with anti-α-tubulin antibodies. Scale bar: 10 µm (A) or 20 µm (B).

Figure 6: Distinct ROS agents differentially impact lysosome motility. RAW cells (A-C, Movies 1-6) or RPE cells (D-F, Movies 7-13) were pre-labelled with Lucifer yellow and exposed to either vehicle, 1 mM H_2O_2 40 min, 1 µM rotenone 60 min, 10 µM CDNB 30 min, 5 µM MCB 30 min, or 5 µM or 10 µM nocodazole for 60 min. Live-cell spinning disc confocal microscopy was performed at a single, mid-cell z-focal plane once every 4 sec for 3 min for RAW cells or every 8 sec for 6 min for RPE cells. Quantification of lysosome speed (A, D), lysosome track length (B, E), and lysosome displacement (C,F) for RAW cells (A-C) or RPE cells (D-F). Data are represented as mean ± s.d. from three independent experiments. One-way ANOVA and Tukey's *post-hoc* test used for B-D, where * indicates P<0.05 between indicated conditions and control. Supplemental Movies 1-13 are representative of the live-cell imaging from which shown data was derived from.

Figure 7: H_2O_2 hinders phagosome-lysosome fusion. (A) RAW cells were treated with H_2O_2 or vehicle (H_2O) for 1h before introducing ZsGreen-expressed *E. coli* (green). RAW cells were incubated for 20 minutes in the presence of bacteria and H_2O_2 or vehicle, then RAW cells were washed with PBS, and further incubated in media containing H_2O_2 or vehicle for an additional 40 minutes. External bacteria were labeled with rabbit anti-*E. coli* antibodies (blue) and were excluded from analysis using a mask. LAMP-1 was labeled with rat anti-LAMP-1 antibodies (red). (B) Quantification of mean LAMP-1 intensity on bacteria-containing phagosomes. LAMP-1 intensities were quantified from regions that co-localized to internal bacteria (green signal and no blue signal). Data represented as a scatter plot, where each dot is an individual phagosome from n = 144 to 179 cells across all independent experiments and conditions. Mean ± standard deviation from three independent experiments is indicated as well. Data analyzed with two-tailed unpaired t-test (* indicates $p<0.05$).

Figure 8: Clathrin inhibition does not arrest ROS-mediated lysosome fragmentation during PIKfyve reactivation. (A) RAW cells were pre-labelled with Lucifer yellow and exposed to either vehicle alone, 1 mM H_2O_2 for 40 min, 1 µM ikarugamcyin for 1 h, or 20 nM apilimod for 60 min. For a subgroup of cells treated with apilimod, drug was replaced with fresh media containing either vehicle, 1 mM H_2O_2, 1 µM ikarugamcyin, or 1 mM H_2O_2 and 1 µM ikarugamycin for 2 h. Fluorescence micrographs are spinning disc microscopy images with 45-55 z-planes represented as z-projections. Scale bar: 5 µm. (B-D) Quantification of individual lysosome volume (B), lysosome number per cell (C), and total lysosome volume per cell (D). Data are shown as mean $\pm$ s.e.m. from three independent experiments, with 25-30 cell assessed

per treatment condition per experiment. One-way ANOVA and Tukey's *post-hoc* test used for B-D, where * indicates $P<0.05$ between experimental and control conditions.

Figure 9: ROS promote actin clearance from lysosomes and actin depolymerization abates lysosomes coalescence during PIKfyve inhibition. (A) RAW cells pre-labelled with Alexa^{488}-conjugated dextran followed by treatment with vehicle, 20 nM apilimod for 40 min alone, or in presence of 10 μM CDNB for 30 min or 1 μM rotenone for 60 min. Cells were fixed with 4% PFA and stained for actin with phalloidin. Fluorescence micrographs were captured by spinning disc confocal as single z-planes. The inset is a magnified portion of field of view tracking Alexa^{488}-conjugated dextran lysosome(s), phalloidin-stained actin, and as merged channels. Scale bar: 2 μm. (B) Cells were assessed for number of actin puncta structures associated with lysosomes. Data represent mean ± S.E.M. from three independent experiments, with 60-80 cells assessed per treatment condition across three experiments. One-way ANOVA and Tukey's *post-hoc* test was used, where * indicates statistical significance between indicated conditions ($p<0.05$). (C) RAW cells were pre-labelled with Lucifer yellow and exposed to vehicle or 20 nM apilimod for 1 h, followed by apilimod removal at 0 or 2 h. These conditions were then supplemented with additional vehicle or 1 μM latrunculin A or 5 μM cytochalasin B for 1 h. Fluorescence micrographs are represented as z-projections of 45-55 z-plane images obtained by spinning disc confocal microscopy. Scale bar: 5 μm. D-F: Quantification of individual lysosome volume (D), lysosome number per cell (E), and total lysosome volume per cell (F). Data represent mean ± S.E.M. from three independent experiments, with 25-30 cells assessed per treatment condition per experiment. One-way ANOVA and Tukey's *post-hoc* test was used, where * indicates statistical significance between indicated conditions ($p<0.05$).

Supplemental Figure S1: ROS accumulation during pharmacological manipulation. (A) RAW cells were exposed to vehicle, or to one of the following treatments – 1 mM H_2O_2 40 min, 1 µM rotenone 60 min, 10 µM CDNB 30 min, or 5 µM MCB 30 min. Cells were then stained with CellROX Green to detect and quantify the levels of ROS formed during these treatments. Additionally, MCB-GSH adduct was also detected during vehicle or MCB treatment (right panels). Fluorescence micrographs represent single z-focal plane images from spinning disc confocal microscopy. Scale bar = 20 µm. (B) Quantification of CellROX Green fluorescence intensity. (C) Quantification of MCB-GSH fluorescence intensity. For both B and C, data are represented as mean $\pm$ S.E.M. from three independent experiments, with 40-50 cells assessed per treatment condition per experiment. One-way ANOVA and Tukey's *post-hoc* test were used for (B), and an unpaired Student's t-test performed for (C). * indicates statistical significance between experimental and control conditions ($P<0.05$).

Supplemental Figure S2: ROS prevent lysosome enlargement during acute PIKfyve suppression in HeLa and RPE cells. (A) HeLa cells pre-labelled with Lucifer yellow and exposed to vehicle or 100 nM apilimod 40 min, or with 1 mM H_2O_2 in the presence or absence of 100 nM apilimod for 40 min. Scale bar: 10 µm. (B-D) Quantification of individual lysosome volume per lysosome (B), lysosome number per cell (C), and total lysosome volume per cell (D). (E) RPE cells pre-labelled with Lucifer yellow and exposed to vehicle, or 1 mM H_2O_2, or 10 µM

CDNB, in presence or absence of 200 nM apilimod 40 min. Scale bar: 20 µm. (F-H) Quantification of individual lysosome volume (F), lysosome number per cell (G), and sum lysosome volume per cell (H). For (B-D) and (F-H), data are represented as mean ± s.e.m. from three independent experiments, with 25-30 cells assessed for (B-D) and 15-20 cells assessed for (F-H) per treatment condition per experiment. One-way ANOVA and Tukey's *post-hoc* test used with **P*<0.05 compared to indicated control conditions.

Supplemental Figure S3: Increased microtubule stability does not affect lysosome motility or lysosome coalescence during PIKfyve inhibition. (A) RAW cells pre-labelled with Lucifer yellow were exposed to either vehicle, or 1 µM or 10 µM paclitaxel for 60 min in presence or absence of 20 nM apilimod for the remaining 40 min. Scale bar: 5 µm. (B-D) Quantification of individual lysosome volume (B), lysosome number per cell (C), and total lysosome volume per cell (D). Data are represented as mean ± s.e.m. from three independent experiments, with 25-30 cell assessed for (B-D) per treatment condition per experiment. (E-G) RAW cells pre-labelled with Lucifer yellow were exposed to vehicle or 1 µM or 10 µM paclitaxel 60 min. Live cell spinning disc confocal microscopy was performed at single z-focal plane once every 4 sec for 3 min. Quantification of lysosome speed (E), lysosome displacement (F), and lysosome track length (G) are shown. Data are represented as mean ± s.d. from three independent experiments. One-way ANOVA and Tukey's *post-hoc* tests were used, where * indicates *P*<0.05 between experimental and control conditions. Data is based on movies like those represented by Movies 14-16.

Supplemental Figure S4. ROS do not affect Rab7 activation and Arl8b loading onto lysosomes. RAW cells expressing RILPC33-GFP (A), or Arl8bWT-GFP (B), exposed to vehicle in absence or presence of 20 nM apilimod 40 min, or 1 mM H_2O_2 40 min in presence or absence of 20 nM apilimod 40 min. Scale bar: 5 µm. (C-D) Quantification of membrane associated fluorescence intensity of RILPC33-GFP (C) from (A) or Arl8bWT-GFP (D) from (B), normalized to cytosol fluorescence intensity. Data represent mean ± s.e.m. from three independent experiments, with 15-20 cell assessed per treatment condition per experiment. One-way ANOVA and Tukey's *post-hoc* test used for C-D with $*P<0.05$ compared to indicated control conditions.

Supplemental Figure S5. H_2O_2 boosts recruitment of clathrin and dynamin to membranes. (A) RPE cells stably expressing clathrin heavy chain-eGFP were pre-labelled with Alexa^{546}-conjugated dextran and treated with vehicle, 1 mM H_2O_2, or 200 nM apilimod with or without 1 mM H_2O_2. Single z- plane images were acquired every 2 min for 40 min across all treatments. Fluorescence micrographs represent single z-plane images at 0 min and 40 min for each treatment obtained by spinning disc microscopy. The inset is a magnified portion of field of view tracking Alexa^{546}-conjugated dextran lysosome(s) or clathrin-eGFP separate or merged. Scale bar: 7 µm. B. Ratio of clathrin-eGFP fluorescence intensities associated with Alexa^{546}-conjugated dextran and cytosol time points: 0, 10, 20, 30, and 40 min. Data are represented as mean ± s.e.m. from five to six independent experiments, with 1-3 cells assessed per treatment condition per experiment. Two-way ANOVA and Tukey's *post-hoc* test were used for (B), where * indicates $P<0.05$ against control conditions. (C) RAW cells were treated with vehicle or 1 mM H_2O_2 for 40 min, lysed and homogenates fractionated through a sucrose gradient

ultracentrifugation. Fractions were immunoblotted against LAMP1 and VAPB to respectively identify lysosome and ER fractions, and aganst clathrin heavy chain and dynamin 2. Protein expression for clathrin heavy chain (D) or dynamin 2 (E) were normalized to LAMP1 for fractions 3 to 6. Data are represented as mean ± s.d. from three independent experiments. Unpaired Student's t-test was used for (D-E), where * indicates $P<0.05$ against vehicle control conditions.

Supplemental Figure S6. Dynamin inhibition does not affect lysosome fragmentation during during PIKfyve reactivation. (A) RAW cells were pre-labelled with Lucifer yellow and exposed to either vehicle, 30 µM dyngo-4A for 2 h, 1 mM H_2O_2 for 40 min, or 1 µM rotenone for 1 h, or 20 nM apilimod for 60 min. Additional subgroup of apilimod treated cells were then washed and incubated with apilimod-free media and changed for 2 h in the presence of vehicle, dyngo-4A, H2O2, and dyngo4-A plus H2O2 for a total time of 2 h without apilimod. Fluorescence micrographs are spinning disc microscopy images with 45-55 z-planes represented as z-projections. Scale bar: 5 µm. (B-D) Quantification of individual lysosome volume (B), lysosome number per cell (C), and total lysosome volume per cell (D). Data is illustrated as mean ± s.e.m. from three independent experiments, with 25-30 cell assessed per treatment condition per experiment. One-way ANOVA and Tukey's *post-hoc* test used for B-D with *$P<0.05$ compared to indicated control conditions.

Supplemental Movie 1: Lysosome motility for vehicle-treated RAW macrophages. Live-cell imaging of RAW macrophages pre-labelled with Lucifer yellow and treated with vehicle-only. Single-plane acquired every 4 sec for 3 min. Time and scale are as indicated.

Supplemental Movie 2: Lysosome motility for H_2O_2-treated RAW macrophages. Live-cell imaging of RAW macrophages pre-labelled with Lucifer yellow and treated with 1 mM H_2O_2 for 40 min. Single-plane acquired every 4 sec for 3 min. Time and scale are as indicated.

Supplemental Movie 3: Lysosome motility for rotenone-treated RAW macrophages. Live-cell imaging of RAW macrophages pre-labelled with Lucifer yellow and treated with 1 μM rotenone for 60 min. Single-plane acquired every 4 sec for 3 min. Time and scale are as indicated.

Supplemental Movie 4: Lysosome motility for CDNB-treated RAW macrophages. Live-cell imaging of RAW macrophages pre-labelled with Lucifer yellow and treated with 10 μM CDNB 30 min. Single-plane acquired every 4 sec for 3 min. Time and scale are as indicated.

Supplemental Movie 5: Lysosome motility for MCB-treated RAW macrophages. Live-cell imaging of RAW macrophages pre-labelled with Lucifer yellow and treated with 5 μM MCB 30 min. Single-plane acquired every 4 sec for 3 min. Time and scale are as indicated.

Supplemental Movie 6: Lysosome motility for nocodazole-treated RAW macrophages. Live-cell imaging of RAW macrophages pre-labelled with Lucifer yellow and treated with 10 μM nocodazole 60 min. Single-plane acquired every 4 sec for 3 min. Time and scale are as indicated.

Supplemental Movie 7: Lysosome motility for vehicle-treated RPE cells. Live-cell imaging of RPE cells pre-labelled with Lucifer yellow and treated with vehicle-only. Single-plane acquired every 8 sec for 6 min. Time and scale are as indicated.

Supplemental Movie 8: Lysosome motility for H_2O_2-treated RPE cells. Live-cell imaging of RPE cells pre-labelled with Lucifer yellow and treated with 1 mM H_2O_2 40 min. Single-plane acquired every 8 sec for 6 min. Time and scale are as indicated.

Supplemental Movie 9: Lysosome motility for rotenone-treated RPE cells. Live-cell imaging of RPE cells pre-labelled with Lucifer yellow and treated with 1 μM rotenone 60 min. Single-plane acquired every 8 sec for 6 min. Time and scale are as indicated.

Supplemental Movie 10: Lysosome motility for CDNB-treated RPE cells. Live-cell imaging of RPE cells pre-labelled with Lucifer yellow and treated with 10 μM CDNB 30 min. Single-plane acquired every 8 sec for 6 min. Time and scale are as indicated.

Supplemental Movie 11: Lysosome motility for MCB-treated RPE cells. Live-cell imaging of RPE cells pre-labelled with Lucifer yellow and treated with 5 μM MCB 30 min. Single-plane acquired every 8 sec for 6 min. Time and scale are as indicated.

Supplemental Movie 12: Lysosome motility for nocodazole five micromolar treated RPE cells. Live-cell imaging of RPE cells pre-labelled with Lucifer yellow and treated with 5 μM nocodazole 60 min. Single-plane acquired every 8 sec for 6 min. Time and scale are as indicated.

Supplemental Movie 13: Lysosome motility for nocodazole ten micromolar treated RPE cells. Live-cell imaging of RPE cells pre-labelled with Lucifer yellow and treated with 10 μM nocodazole 60 min. Single-plane acquired every 8 sec for 6 min. Time and scale are as indicated.

Supplemental Movie 14: Lysosome motility for vehicle-treated RAW macrophages. Live-cell imaging of RAW cells pre-labelled with Lucifer yellow and treated with vehicle-only. Single-plane acquired every 4 sec for 3 min. Time and scale are as indicated.

Supplemental Movie 15: Lysosome motility for paclitaxel one micromolar treated RAW macrophages. Live-cell imaging of RAW cells pre-labelled with Lucifer yellow and treated with 1 μM paclitaxel 60 min. Single-plane acquired every 4 sec for 3 min. Time and scale are as indicated.

Supplemental Movie 16: Lysosome motility for paclitaxel ten micromolar treated RAW macrophages. Live-cell imaging of RAW cells pre-labelled with Lucifer yellow and treated with 10 μM paclitaxel 60 min. Single-plane acquired every 4 sec for 3 min. Time and scale are as indicated.

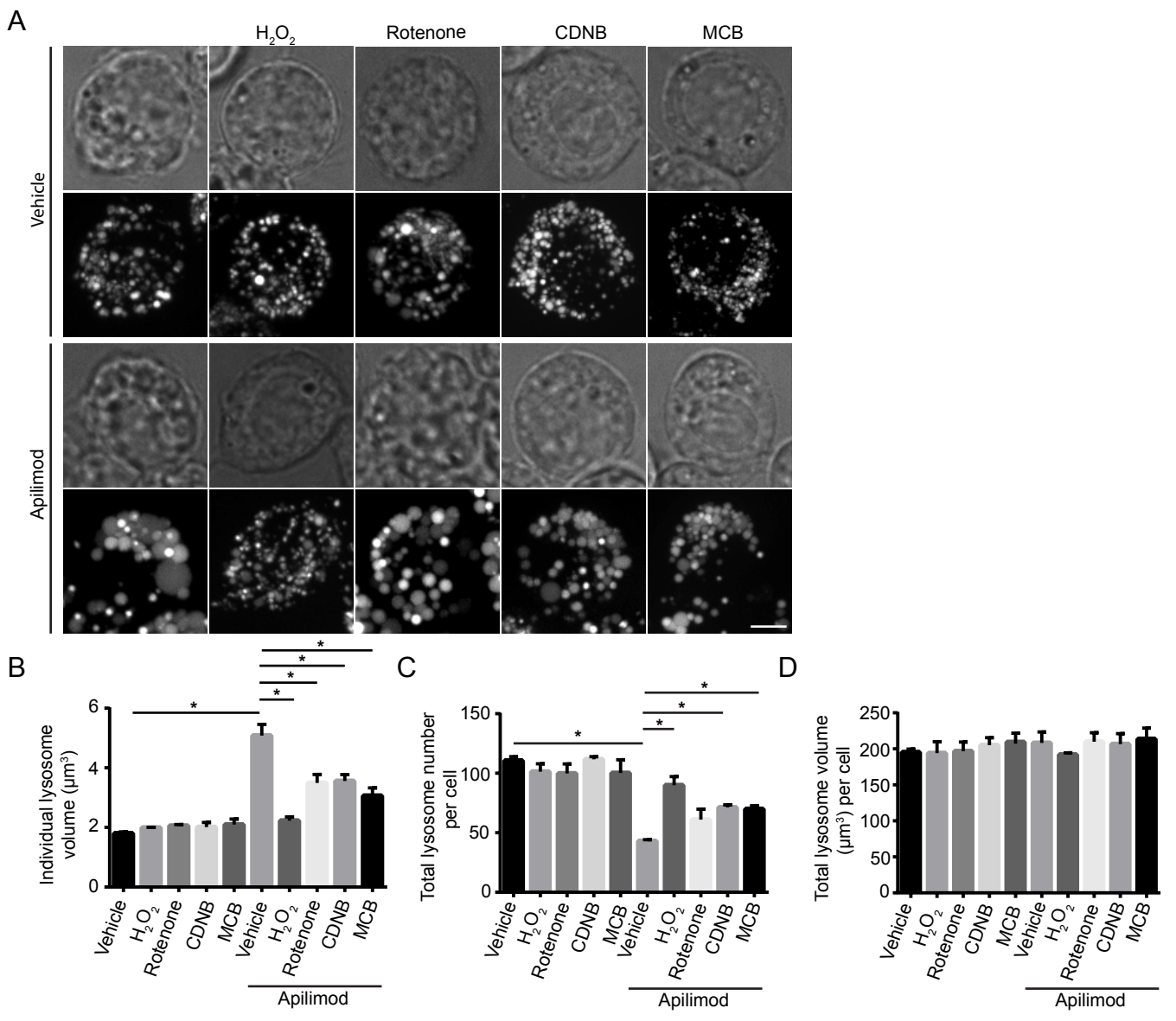
A
H2O2
Rotenone
CDNB
MCB
Vehicle
Apilimod
B
Individual lysosome volume (μm3)
Vehicle
H2O2
Rotenone
CDNB
MCB
Apilimod
C
Total lysosome number per cell
D
Total lysosome volume (μm3) per cell

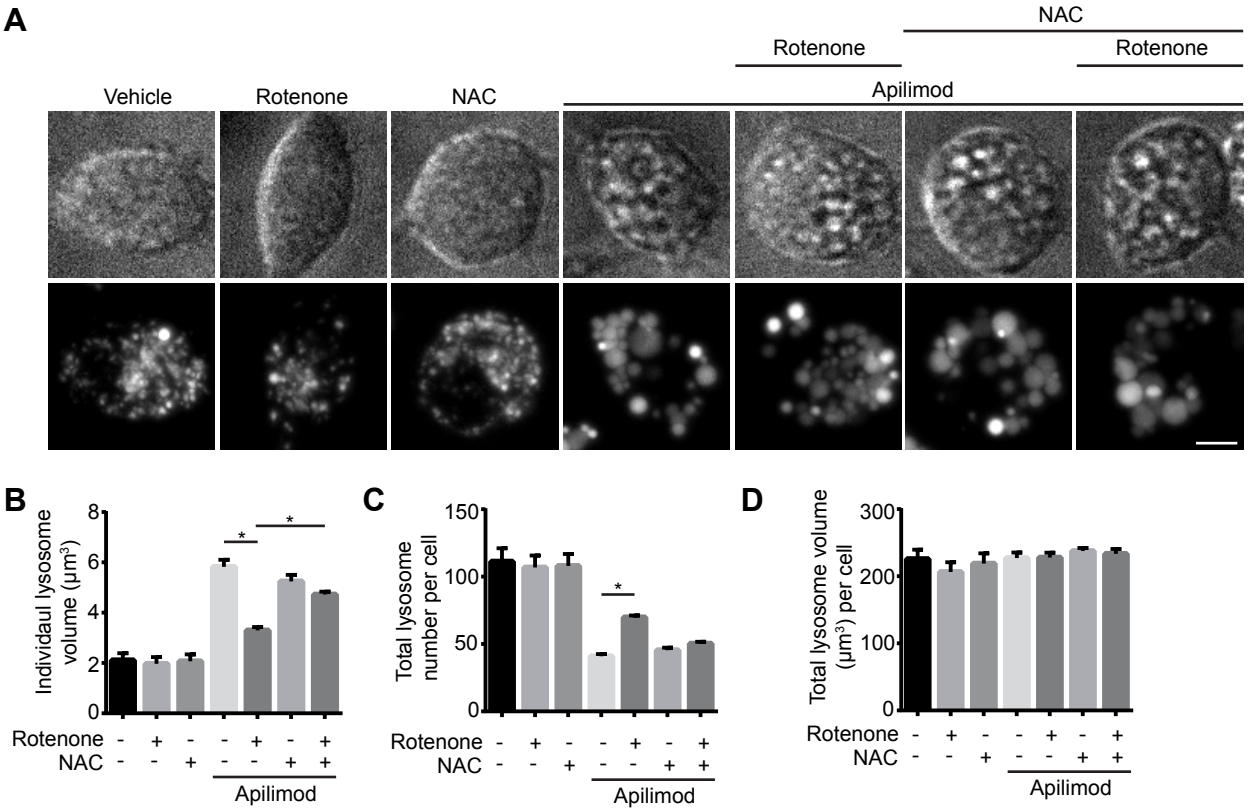
A
NAC
Rotenone
Rotenone
Vehicle
Rotenone
NAC
Apilimod
B
Individaul lysosome volume (μm³)
8
6
4
2
0
*
*
Rotenone - + - - + - +
NAC - - + - - + +
Apilimod
C
Total lysosome number per cell
150
100
50
0
*
Rotenone - + - - + - +
NAC - - + - - + +
Apilimod
D
Total lysosome volume (μm³) per cell
300
200
100
0
Rotenone - + - - + - +
NAC - - + - - + +
Apilimod

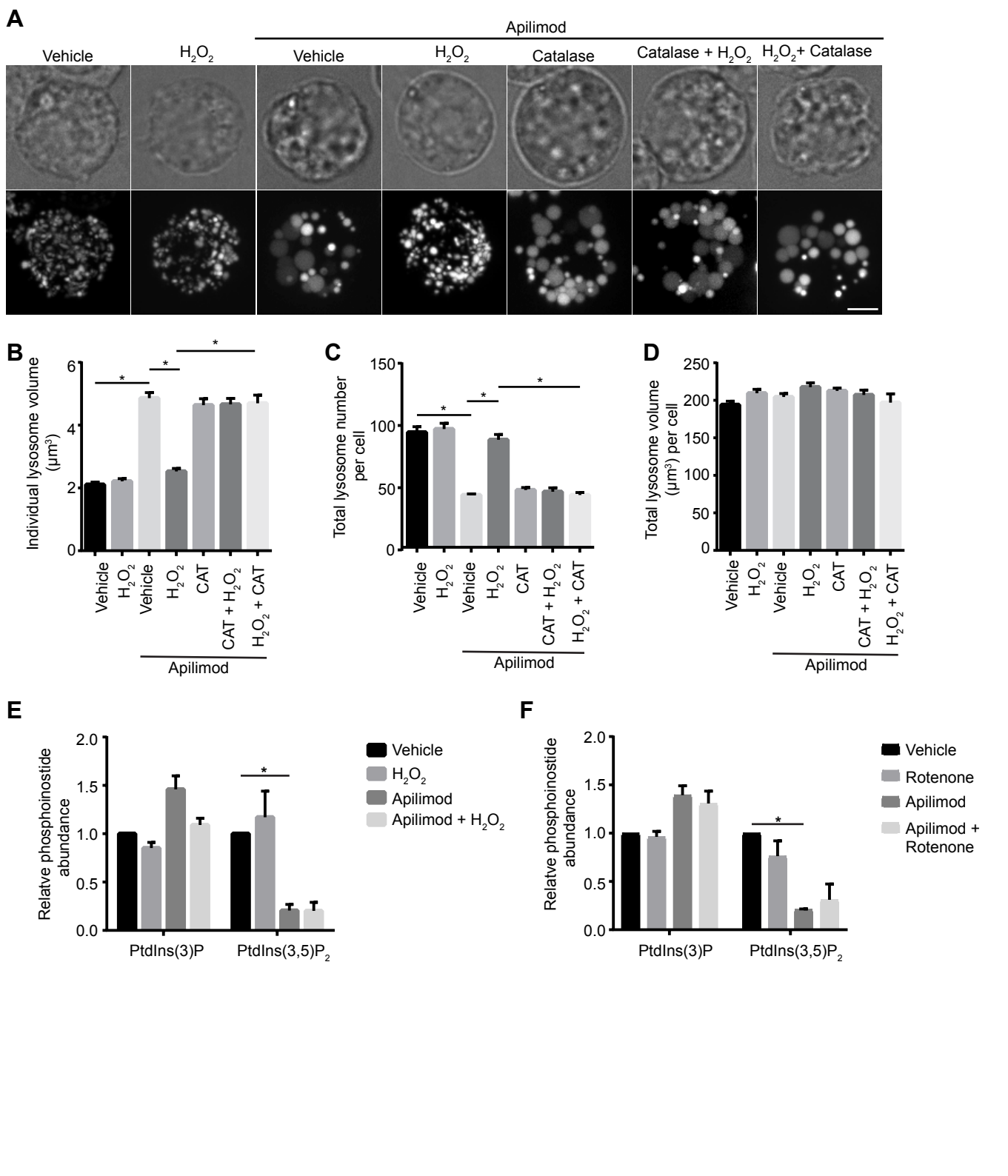
A
Apilimod
Vehicle
H2O2
Vehicle
H2O2
Catalase
Catalase + H2O2
H2O2+ Catalase
B
Individual lysosome volume (µm3)
Vehicle
H2O2
Vehicle
H2O2
CAT
CAT + H2O2
H2O2 + CAT
Apilimod
C
Total lysosome number per cell
Vehicle
H2O2
Vehicle
H2O2
CAT
CAT + H2O2
H2O2 + CAT
Apilimod
D
Total lysosome volume (µm3) per cell
Vehicle
H2O2
Vehicle
H2O2
CAT
CAT + H2O2
H2O2 + CAT
Apilimod
E
Relatve phosphoinostide abundance
PtdIns(3)P
PtdIns(3,5)P2
Vehicle
H2O2
Apilimod
Apilimod + H2O2
F
Relatve phosphoinostide abundance
PtdIns(3)P
PtdIns(3,5)P2
Vehicle
Rotenone
Apilimod
Apilimod + Rotenone

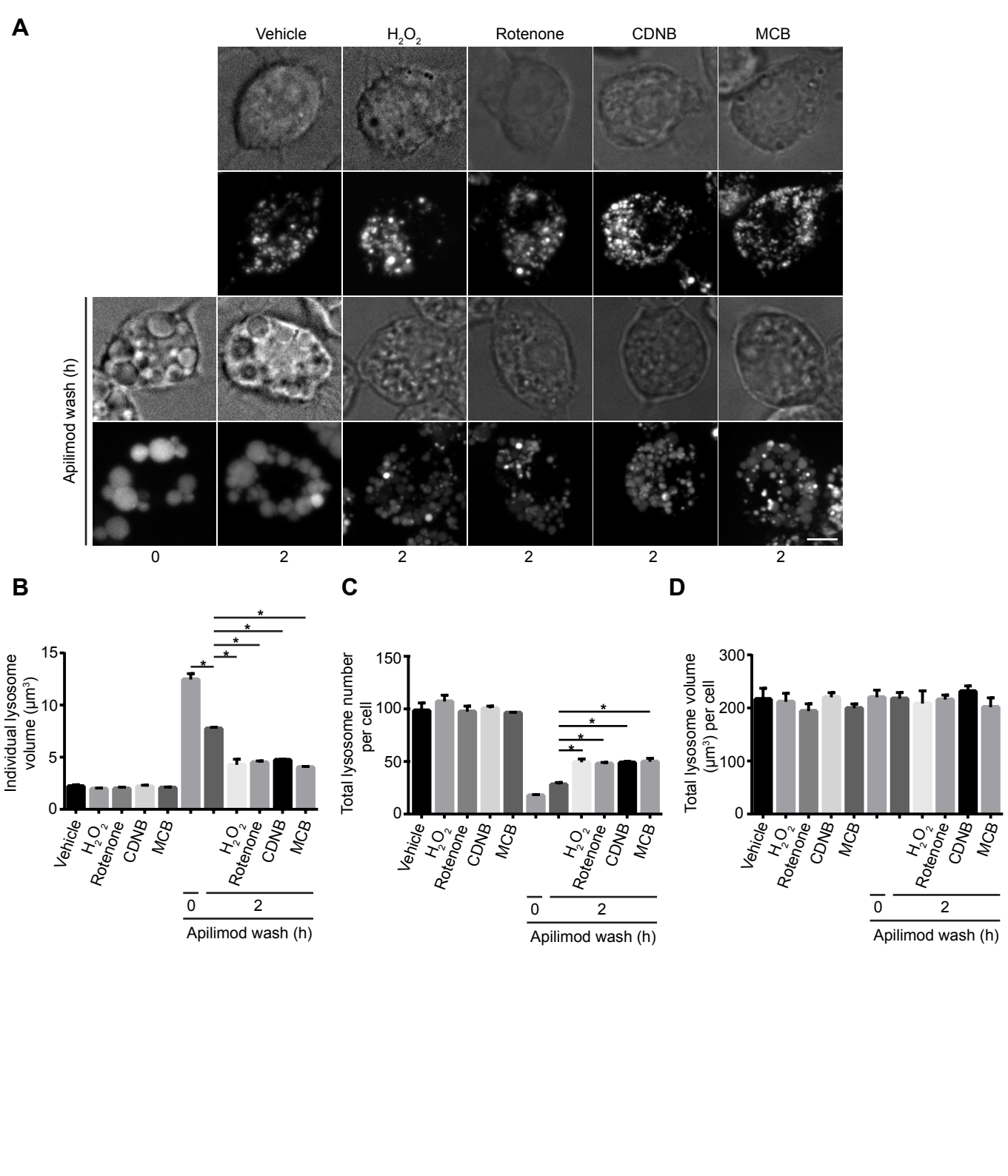
A
Vehicle
H2O2
Rotenone
CDNB
MCB
Apilimod wash (h)
0
2
2
2
2
2
B
Individual lysosome volume (μm3)
15
10
5
0
Vehicle
H2O2
Rotenone
CDNB
MCB
H2O2
Rotenone
CDNB
MCB
0
2
Apilimod wash (h)
C
Total lysosome number per cell
150
100
50
0
Vehicle
H2O2
Rotenone
CDNB
MCB
H2O2
Rotenone
CDNB
MCB
0
2
Apilimod wash (h)
D
Total lysosome volume (μm3) per cell
300
200
100
0
Vehicle
H2O2
Rotenone
CDNB
MCB
H2O2
Rotenone
CDNB
MCB
0
2
Apilimod wash (h)

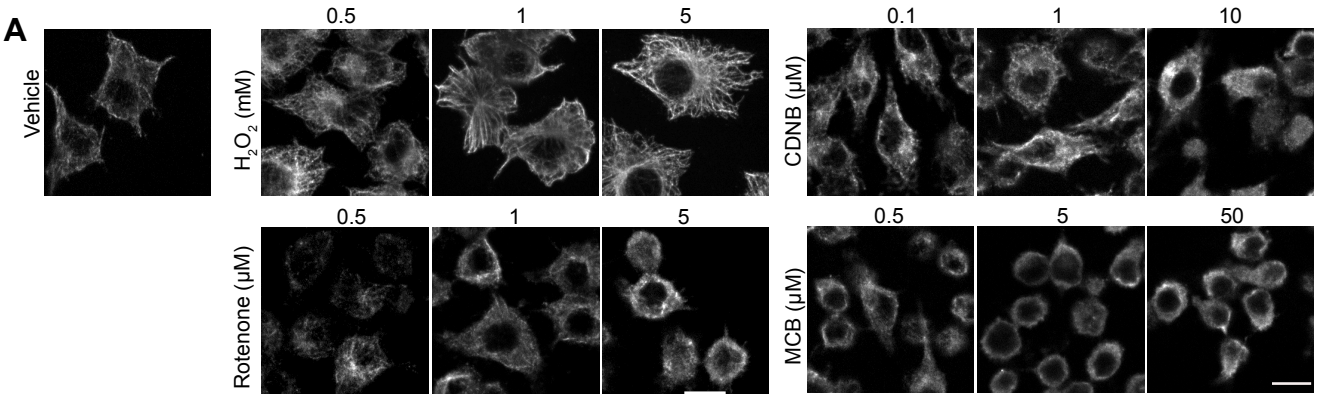
A
Vehicle
0.5
1
5
H2O2 (mM)
0.1
1
10
CDNB (μM)
0.5
1
5
Rotenone (μM)
0.5
5
50
MCB (μM)

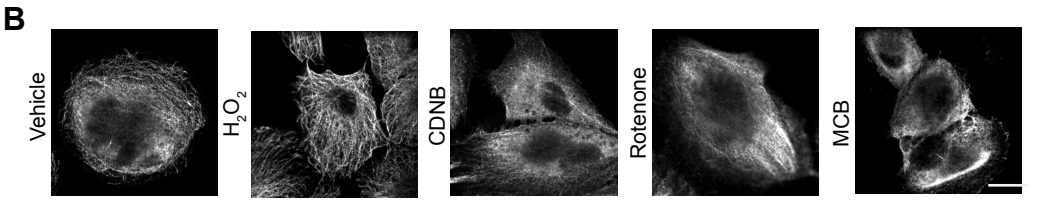
B
Vehicle
H2O2
CDNB
Rotenone
MCB

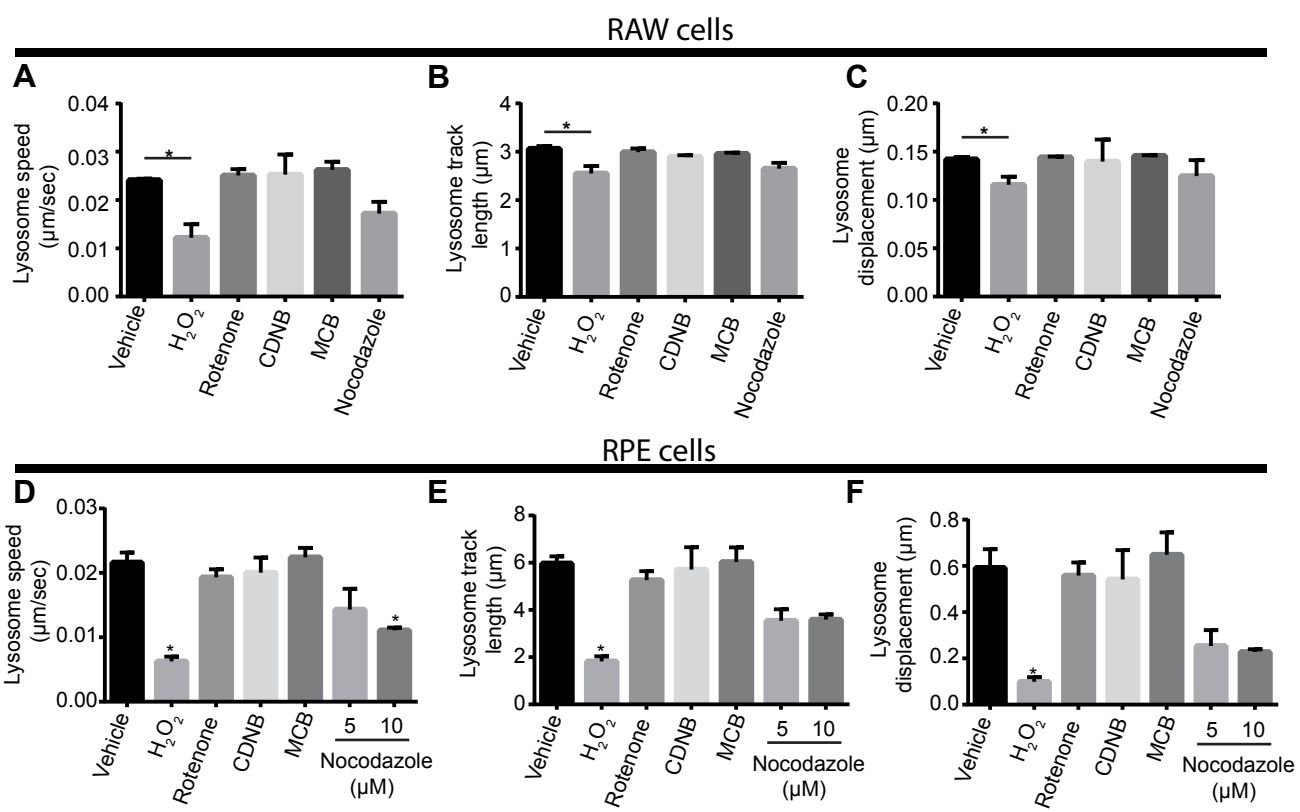
RAW cells
A
Lysosome speed (μm/sec)
0.04
0.03
0.02
0.01
0.00
*
Vehicle
H2O2
Rotenone
CDNB
MCB
Nocodazole
B
Lysosome track length (μm)
4
3
2
1
0
*
Vehicle
H2O2
Rotenone
CDNB
MCB
Nocodazole
C
Lysosome displacement (μm)
0.20
0.15
0.10
0.05
0.00
*
Vehicle
H2O2
Rotenone
CDNB
MCB
Nocodazole
RPE cells
D
Lysosome speed (μm/sec)
0.03
0.02
0.01
0.00
*
*
Vehicle
H2O2
Rotenone
CDNB
MCB
5
10
Nocodazole (μM)
E
Lysosome track length (μm)
8
6
4
2
0
*
Vehicle
H2O2
Rotenone
CDNB
MCB
5
10
Nocodazole (μM)
F
Lysosome displacement (μm)
0.8
0.6
0.4
0.2
0.0
*
Vehicle
H2O2
Rotenone
CDNB
MCB
5
10
Nocodazole (μM)

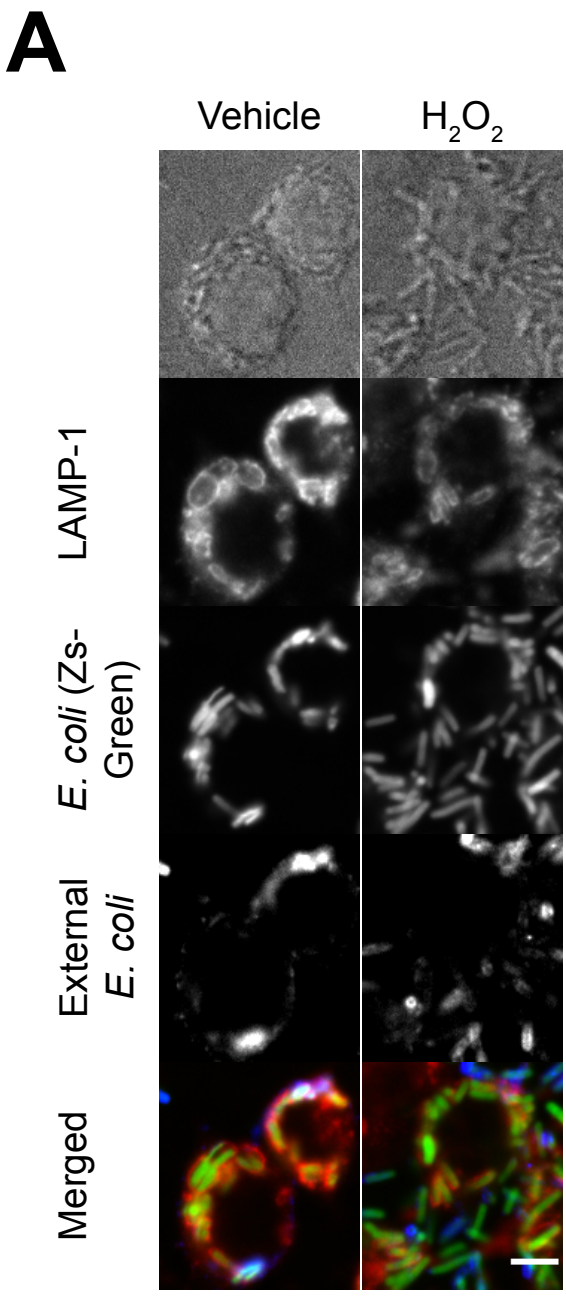
A
Vehicle
H2O2
LAMP-1
E. coli (Zs-Green)
External E. coli
Merged
B
Mean LAMP-1 Fluorescence
15000
10000
5000
0
*
Vehicle
H2O2

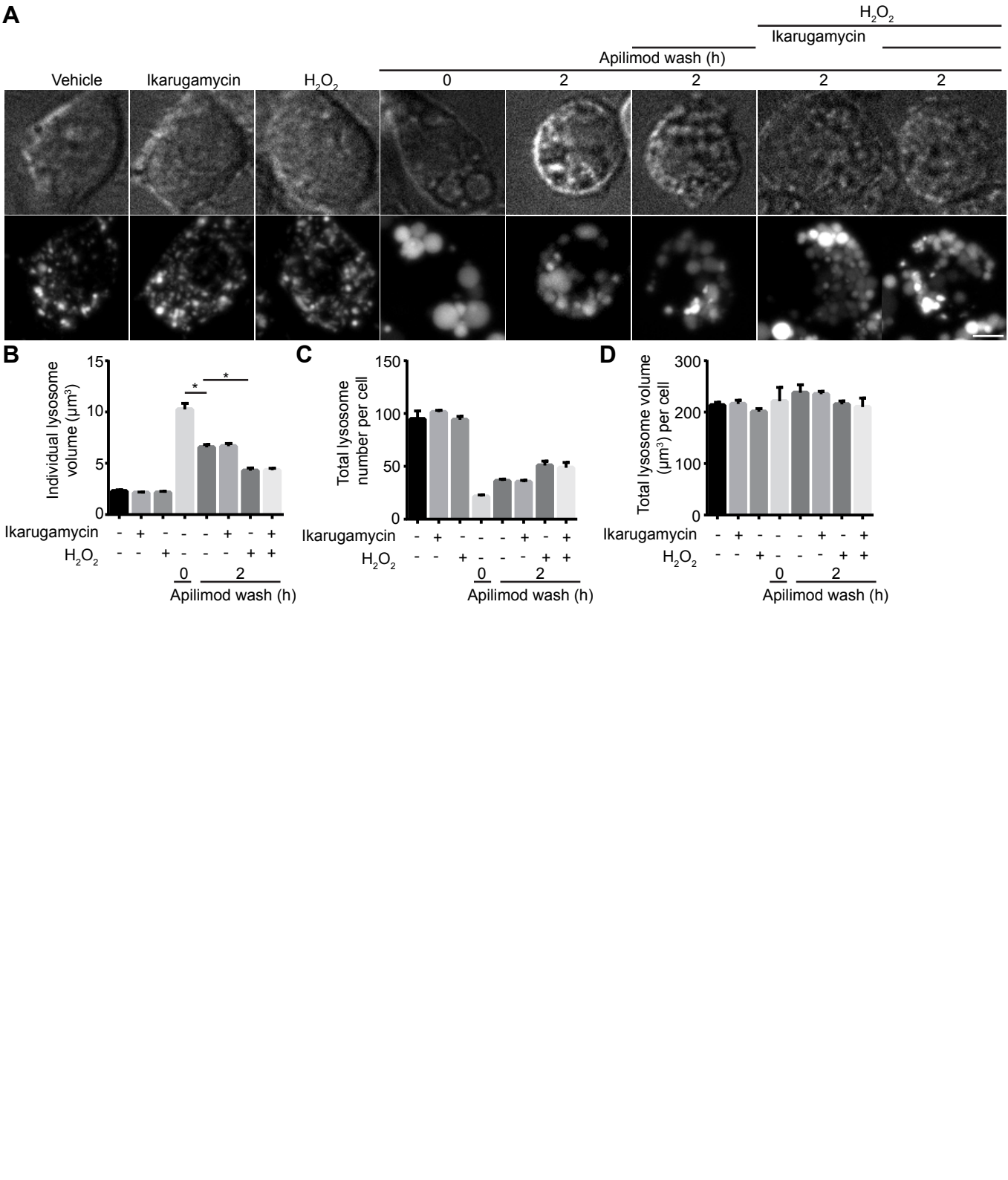
A
H2O2
Ikarugamycin
Apilimod wash (h)
Vehicle
Ikarugamycin
H2O2
0
2
2
2
2
B
Individual lysosome volume (µm3)
15
10
5
0
*
*
Ikarugamycin - + - - - + - +
H2O2 - - + - - - + +
0
2
Apilimod wash (h)
C
Total lysosome number per cell
150
100
50
0
Ikarugamycin - + - - - + - +
H2O2 - - + - - - + +
0
2
Apilimod wash (h)
D
Total lysosome volume (µm3) per cell
300
200
100
0
Ikarugamycin - + - - - + - +
H2O2 - - + - - - + +
0
2
Apilimod wash (h)

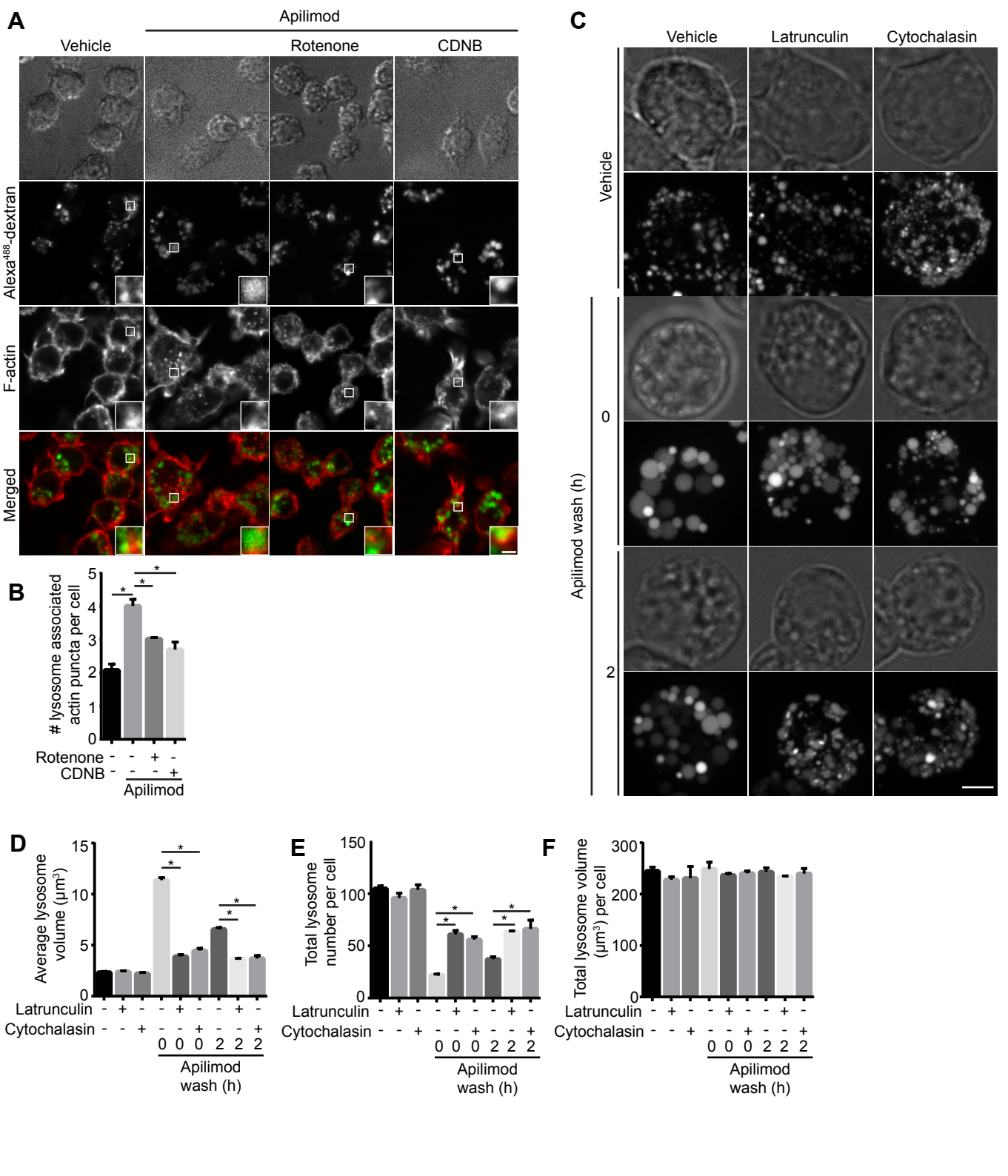
A
Apilimod
Vehicle
Rotenone
CDNB
Alexa488-dextran
F-actin
Merged
B
lysosome associated actin puncta per cell
Rotenone
CDNB
Apilimod
C
Vehicle
Latrunculin
Cytochalasin
Vehicle
Apilimod wash (h)
0
2
D
Average lysosome volume (μm3)
Latrunculin
Cytochalasin
Apilimod wash (h)
E
Total lysosome number per cell
Latrunculin
Cytochalasin
Apilimod wash (h)
F
Total lysosome volume (μm3) per cell
Latrunculin
Cytochalasin
Apilimod wash (h)